UNIVERSITY OF OKLAHOMA GRADUATE COLLEGE

PULSED LASER DEPOSITION AND OPTIMIZATION OF LSGM AND LSCF THIN FILMS FOR SOLID OXIDE FUEL CELL APPLICATIONS

A THESIS

SUBMITTED TO THE GRADUATE FACULTY

in partial fulfillment of the requirements for the

Degree of

MASTER OF SCIENCE

By ADAM GOLDBERG

Norman, Oklahoma

2025

PULSED LASER DEPOSITION AND OPTIMIZATION OF LSGM AND LSCF THIN FILMS

FOR SOLID OXIDE FUEL CELL APPLICATIONS

A THESIS APPROVED FOR THE
SCHOOL OF AEROSPACE AND MECHANICAL ENGINEERING

BY THE COMMITTEEE CONSISTING OF

Dr. Iman Ghamarian, Chair

Dr. Hanjong Paik

Dr. Pejman Kazempoor

© Copyright by ADAM GOLDBERG 2025
All Rights Reserved.

Acknowledgements

I would like to express my deepest gratitude to **Dr. Hanjong Paik** for his invaluable guidance throughout this project, and for teaching me the fundamentals and advanced concepts of pulsed laser deposition (PLD).

I am also sincerely thankful to **Dr. Iman Ghamarian** for his constant support and for securing the fuel cell materials essential to this work.

Special thanks to **Sooraj Patel** for introducing me to this project, clearly explaining the research goals, and assisting with SEM characterization.

I am grateful to **Dr. Pralay Paul** for his mentorship in the lab, teaching me how to operate our PLD system and helping me interpret XRD data.

Thank you to **Dr. Sumit Goswami** for his assistance with XRD measurements and support in the target preparation process, and electrical characterization process.

I also extend my appreciation to **Dr. Venky and the PLD Lab Team** for allowing me to use the PLD lab space and powder fabrication facilities, and for their continuous support.

A special thanks to the **SRNML team** for their expertise and assistance with XRD measurements and SEM.

Finally, I would like to thank **Sen Seymour** for his support and camaraderie throughout both our undergraduate and graduate journeys.

Abstract

The performance and durability of solid oxide fuel cells (SOFCs) are critically governed by the structural and chemical coherency of the hetero-interfaces between oxygen ion-conducting electrolytes and electronically conducting electrodes. In particular, realizing coherent and chemically stable interfaces between $La_{0.8}Sr_{0.2}Ga_{0.8}Mg_{0.2}O_{3-\delta}$ (LSGM), a fast oxygen-ion conductor, and $(La_{0.6}Sr_{0.4})_{0.95}Co_{0.2}Fe_{0.8}O_{3-\delta}$ (LSCF), a mixed ionic-electronic conductor, is critical for minimizing interfacial resistance and enabling high-efficiency energy conversion.

A major challenge in solid-state fuel cells arises from the potential interdiffusion of cations across electrolyte/electrode interfaces, which can lead to the formation of undesired secondary phases and degraded ionic/electronic transport properties. Therefore, precise interface engineering is essential to preserve the functional stability of both layers. Despite the technological importance, detailed experimental studies remain lacking, especially on the epitaxial growth and hetero-interface structure of LSGM and LSCF heterostructures using Pulsed Laser Deposition (PLD).

In this work, we systematically optimized PLD growth conditions for single-crystalline LSGM and LSCF thin films on $SrTiO_3$ (001) substrates, aiming to establish a coherent and well-defined hetero-interface suitable for fundamental studies of interfacial phenomena under the fuel cell operating condition. X-ray diffraction (XRD) analysis revealed that LSGM films grown at 800 °C and 150 mTorr of oxygen partial pressure exhibited a lattice parameter of 3.909 Å (±0.017) with a full-width-at-half-maximum (FWHM) of 0.169°, while LSCF films grown under optimized conditions showed a lattice parameter of 3.916 Å (±0.021) and an FWHM of 0.072°, indicating high crystallinity and epitaxial alignment. As a result, the successful fabrication of LSGM/LSCF heterostructure exhibited distinct XRD peaks from both layers, suggesting layered epitaxial growth without significant interdiffusion or secondary phase formation under the optimized conditions.

This study provides a reproducible route for the coherent integration of LSGM electrolytes and LSCF electrodes via PLD, offering a model platform for exploring interfacial transport, defect chemistry, and long-term stability — essential aspects for the development of next-generation, high-performance SOFC devices.

Table of Contents

List of Figures

List of Tables

Chapter 1: Introduction

1.1 Overview of Solid Oxide Fuel Cells

Solid oxide fuel cells (SOFCs) are high-temperature electrochemical devices that convert fuel and oxygen into electricity via ionic conduction. A typical SOFC consists of a dense oxide electrolyte in between an anode and cathode. At the anode side, fuel (e.g. H_2 or CO) is oxidized by O^{2-} ions from the electrolyte (e.g. $H_2 + O^{2-} \rightarrow H_2O + 2e^-$), releasing electrons to an external circuit. At the cathode side, the returning electrons reduce oxygen from air ($\frac{1}{2}O_2 + 2e^- \rightarrow O^{2-}$), and the resulting oxide ions migrate through oxygen vacancies in the electrolyte to sustain the reaction. This separation of ionic and electronic pathways forces electrons through the load, producing power, while the oxygen-ion conduction in the electrolyte completes the internal circuit. The overall reaction produces water (or CO_2 when using carbonaceous fuels) and heat, due to the SOFC process being exothermic.

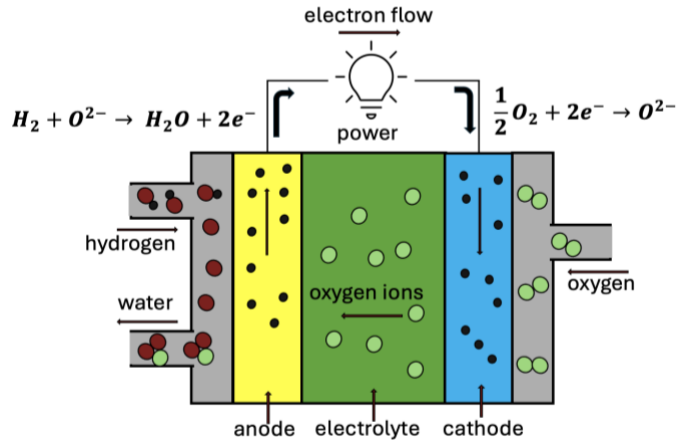

Figure 1: SOFC process overview

SOFCs offer high efficiency and fuel flexibility for clean energy conversions, but conventional SOFCs require high operating temperatures (~800-1000°C). High operating temperatures not only

lengthen startup times, but can also lead to material degradation, chemical instability, and delamination between layers in high thermal expansion mismatch situations. On a broad scale, the goal of this study is to study the intrinsic properties of electrolyte and cathode materials to allow for advancement in fuel cell materials.

1.1.1 SOFC Material Selection

The electrolyte's role is to conduct O^{2-} ions from the cathode to anode while preventing electrons from passing through. Thus, electrolyte materials typically have high oxygen-ion conductivity and negligible electronic conductivity. In oxide electrolytes like yttria-stabilized zirconia (YSZ), oxygen ions move by hopping between vacant anion sites. Historically, YSZ has been the industry standard electrolyte material[1]. Doping with Y_2O_3 introduces oxygen vacancies that serves as carriers, and once thermally activated (traditionally 800-1000°C) sufficient ion conductivity can be sustained. At these temperatures, ohmic losses in the electrolyte are low, but significant heat is generated through the electrochemical reactions and internal resistances. Excess heat can be removed via heat exchangers to help preheat reactants and maintain a more uniform temperature distribution to avoid material cracking.

Although YSZ has been the standard SOFC electrolyte for decades, the discovery of $La_{0.8}Sr_{0.2}Ga_{0.8}Mg_{0.2}O_{3-\delta}$ (LSGM) significantly improved oxygen ion conductivity, enabling lower-temperature SOFC operation [2-4]. Bulk LSGM fuel cells also have challenges, mainly concerning secondary phase formation. Achieving a dense, single-phase LSGM ceramic requires high sintering temperatures (~1400-1500°C), leading to secondary phases like $LaSrGa_3O_7$ or $LaSrGaO_4$[5-8]. Both of these secondary phases are insulative or have negligible ionic conductivity, leading to poor SOFC performance [5]. By fabricating an electrolyte as a single

crystal thin film, one can observe the intrinsic lattice ionic conductivity of LSGM without the influence of grain boundaries or secondary phases.

On a traditional cathode like $La_{1-x}Sr_xMnO_3$ (LSM), which is primarily an electronic conductor, O^{2-} ions can only be produced at the triple-phase boundaries (TPBs) where, gas, electrolyte, and electrode meet[5]. In contrast, on mixed ionic-electronic conductors (MIECs) such as $(La_{0.6}Sr_{0.4})_{0.95}Co_{0.2}Fe_{0.8}O_{3-\delta}$ (LSCF), oxygen ions can diffuse through the cathode itself, extending the reaction zone beyond only the TPBs[9-10]. LSCF became a popular cathode for intermediate temperatures because it exhibits mixed ionic and electronic conductivity and much higher oxygen reduction activity than traditional LSM cathodes at the 400-800°C range [10]. A typical LSCF cathode is polycrystalline, suffering Sr segregation with long term operation[11]. Sr segregation occurs when SrO or $SrCO_3$ forms at the surface degrading catalytic activity. By studying LSCF as an epitaxial film, one can eliminate the ambiguities of a porous composite microstructure and focus directly on the intrinsic properties (electronic and ionic conductivity) under well controlled strain states. Insights on how single crystal LSCF strain states affect these properties could be implemented in SOFCs allowing for prolonged activity.

1.1.2 SOFC Fabrication Techniques

Early SOFCs and many modern ones are made by pressing or casting ceramic powders into layers and sintering them at high temperatures. For example, electrolyte disks can be made by pressing YSZ powder, then sintering at ~1400°C to achieve a dense pellet. Tape casting is another common method used to create sheets of electrolyte which are then also sintered to achieve high density. Porous electrodes like $NiO-YSZ$ anode or LSM cathode can be screen-printed onto the electrolyte directly and sintered. These layers can be sintered in separate steps, or co-sintered for lower cost mass production. Another coating method used to deposit electrolyte or electrode layers include

slurry/suspension coating, where a paste of ceramic particles is deposited by printing, dip-coating, or spin-coating onto a substrate and then sintered. These methods can produce electrolyte films on the order of 10-100 microns. Electrophoretic deposition (EPD) is a wet technique using an electric field to deposit charged particles onto a substrate and has been used to make thinner film electrolyte layers. Although these techniques are effective for making micron layer thickness film layers, then still rely on high temperatures sintering to create high density films (increasing risks of secondary phases and thermal expansion cracking). For larger area cells or rapid fabrication, methods like plasma spraying can directly deposit ceramic layers by flame-heating and propelling powder onto a substrate.

1.2 Characterization Methods

Before the SOFC is fabricated, individual layer materials are characterized using a range of techniques to verify phase purity and overall integrity of the material. Similar characterization steps are taken after the SOFC is assembled, as well as overall performance characterization.

Once fabricated, solid oxide fuel cell materials and cells undergo extensive characterization using a variety of techniques to assess their structural, electrical, and electrochemical properties. One of the primary methods is electrical performance testing, where the voltage–current (V–I) polarization curve is measured to determine the power density of the cell. Key performance metrics include the open-circuit voltage (which ideally approaches the Nernst potential, indicating minimal leakage) and the maximum power density. For instance, an anode-supported SOFC with an LSGM electrolyte and an LSCF cathode can achieve power densities exceeding 2 W/cm² at 700°C, whereas a similar cell with a thicker, printed electrolyte may reach only around 1 W/cm² [12]. Such comparisons illustrate how fabrication parameters directly influence SOFC performance, highlighting the importance of optimizing material thickness and microstructure.

Another critical technique is electrochemical impedance spectroscopy (EIS), which is widely used to deconvolute resistive losses within the SOFC. By analyzing impedance over a range of frequencies, EIS can separate ohmic resistance (primarily from the electrolyte) from polarization resistances associated with the anode and cathode processes. A typical SOFC impedance spectrum includes a high-frequency intercept corresponding to the electrolyte's ohmic resistance and one or more arcs at lower frequencies that relate to electrode kinetics. EIS is especially useful for diagnosing rate-limiting processes and evaluating improvements in material design. For example, a thin-film electrolyte results in significantly lower ohmic resistance, while a newly engineered cathode material may exhibit reduced polarization resistance at mid frequencies [13,14]. As the push for lower-temperature SOFCs intensifies, there is increasing emphasis on minimizing both types of resistance—through the development of thinner, more conductive electrolytes and more active electrode materials.

Beyond electrochemical characterization, microstructural and phase characterization techniques provide essential insights into the crystallinity and morphology of SOFC materials. X-ray diffraction (XRD) is a fundamental tool for verifying phase purity and crystal structure, ensuring that materials such as LSGM exhibit the desired cubic perovskite phase without secondary phases like $LaSrGaO_4$, which could indicate processing issues [5]. Scanning electron microscopy (SEM) is widely used to examine the microstructure of sintered electrolytes and electrodes, revealing features such as grain size in YSZ electrolytes or the porosity and connectivity of Ni-YSZ anodes. Additionally, energy-dispersive X-ray spectroscopy (EDS) can map element distributions, detecting potential issues like Sr migration to the cathode surface. At a more advanced level, transmission electron microscopy (TEM) enables researchers to examine interfaces, such as the

electrolyte/cathode interface, where reaction products or lattice strain could impact the performance.

Overall, the characterization of SOFC materials is essential for validating fabrication improvements. The development of thinner, denser electrolytes or engineered composite electrodes must be matched with thorough performance verification, ensuring enhanced conductivity and overall cell efficiency. The combination of electrochemical, structural, and mechanical characterization techniques has been instrumental in advancing SOFC technology, particularly as new materials like LSGM and LSCF continue to be explored. These characterization methods not only aid in optimizing processing conditions but also contribute to a deeper understanding of material behavior, ultimately driving the development of more efficient and durable SOFCs.

1.3 Strain Engineering in SOFCs

Apart from changing the composition, or doping, strain can be a powerful tool to engineer the properties of a SOFC material. Strain can be introduced intentionally through intentional mismatch between layers or can arise during operation as a result of thermal expansion. In both cases, elastic strain can alter properties like ionic conductivity, catalytic activity, and even the electronic structure of oxide materials.

The mobility of oxygen vacancies in an ionic solid is sensitive to the crystal lattice environment. Imposing strain on a lattice changes interatomic distances (a, b, c) and the potential energy landscape created by atomic nuclei. This can greatly impact the ability of diffusing ions to traverse through the material. One example in electrolyte materials is with YSZ thin films: when YSZ is grown epitaxially on a substrate of larger lattice constant, its ionic conductivity increases beyond the bulk value [15]. Jiang found that thin YSZ films under tensile strain showed lower activation

energy and higher ionic conductivity than thicker relaxed films, or bulk YSZ. In this case, tensile strain opened up oxygen vacancy channels slightly by increasing edge dislocation density in the single crystal[15]. Similar studies on ceria and other fluorites indicate that tensile strain can increase ionic conductivity by increasing vacancy concentration or mobility along edge dislocations.

Although tensile strain in YSZ thin films boosts ionic conductivity, the effect of strain on conductivity seems to be asymmetric and different for many materials. YSZ in moderate compressive strain was found to have negligible change in overall ionic conductivity[16]. In a Li-ion conductor the relationship is inversely proportional, as compressive strain along an axis greatly increased ionic conductivity, whereas tensile strain in the same direction decreased it. Regardless of the complexity of this relation, designing thin-film structures and testing under different strain states can be a deliberate strategy to achieve better ionic conductivity properties for SOFCs.

1.4 Pulsed Laser Deposition (PLD) in SOFC Fabrication

Pulsed Laser Deposition (PLD) has become an invaluable tool in the fabrication of advanced SOFC materials, especially for research-scale cells and fundamental investigations. PLD is a physical vapor deposition technique wherein a high-energy pulsed laser beam is focused onto a target material, causing it to ablate and form a plasma plume. This plume contains a stoichiometric vapor of the target, which expands and deposits onto a substrate, typically held at elevated temperature in a controlled atmosphere [17]. The result is a thin film that can closely reproduce the target's composition. Below is an outline the working principles of PLD, its advantages, and how growth conditions are optimized to achieve high-quality films that enhance SOFC performance.

In a PLD chamber, a laser (often an excimer UV laser like KrF, 248 nm) is pulsed (e.g. 1–10 Hz) and each pulse delivers a burst of energy to the target surface. The rapid heating causes material to evaporate as an energetic plasma. The key aspect is that even complex oxide targets (containing multiple cations) can be evaporated in a way that the film stoichiometry matches the target [17]. The substrate is placed facing the target at some distance (a few cm) and can be heated (anywhere from room temperature to >800 °C) depending on the desired film crystallinity. The chamber can be evacuated or backfilled with a gas (often O_2 for oxide films). By adjusting the oxygen background pressure, one can influence the plume dynamics and also ensure the deposited film grows in an oxygen-rich environment to form the correct oxide phases. PLD typically produces deposition rates on the order of 0.05–1 Å per laser pulse, allowing growth of nm-scale layers with great precision [17]. In situ monitoring techniques like RHEED (reflection high-energy electron diffraction) can be used during PLD to observe the film's growth mode and crystallinity in real time, which is valuable for research on epitaxial films.

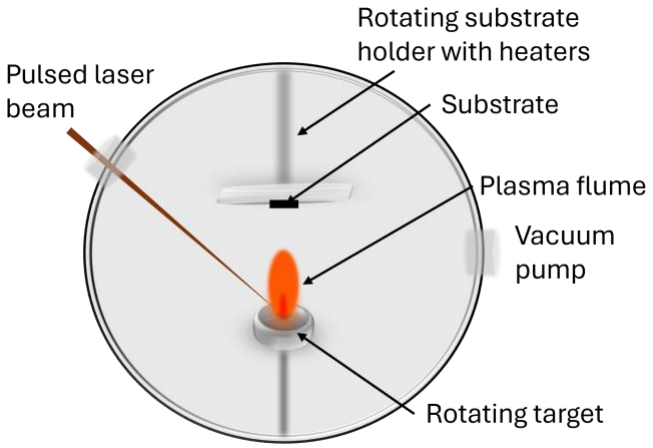

Figure 2: PLD process diagram

One of PLD's biggest advantages is its ability to transfer complex compositions from target to film. For materials like LSCF or LSGM, which have four elements and volatile constituents (e.g.

Ga, which can evaporate easily), maintaining the right cation ratio is non-trivial with other methods. PLD's rapid ablation and quenching of material on the substrate helps preserve the target's stoichiometry in the film.

PLD can be done in high vacuum or in a partial pressure of gas. This is crucial for oxides; typically, a few to hundreds of mTorr of O_2 is introduced so that the film grows in an oxidizing environment. This flexibility allows making either fully oxygenated films or oxygen-deficient films (by using low pressure or even inert gas). For SOFC, one often wants fully oxidized structures (e.g. no oxygen vacancies beyond the stable δ in LSCF). Because the substrate can be heated and because the ablated species are energetic (often arriving with tens of eV of kinetic energy), PLD can produce highly crystalline films, including epitaxial layers on single-crystal substrates. Epitaxial growth means the film is a single crystal aligned to the substrate lattice. This is extremely useful for fundamental studies – for example, growing an epitaxial LSGM film on a perovskite substrate to study inherent conductivity, or growing an LSCF film on YSZ to probe the interface structure. It also is the way to achieve the strain engineering discussed earlier (by deliberately choosing substrate lattice parameters to impose strain on the film).

PLD's stop-start nature (pulse-by-pulse) and ability to use multiple targets in sequence make it easy to fabricate layered structures. One can deposit an electrolyte film then switch to a cathode target and deposit a cathode film without breaking vacuum, creating a clean interface. This is used in making model thin-film cells or heterostructures (for instance, an LSCF|LSM bilayer cathode, or grain-boundary model structures with alternating layers). The interfaces made by PLD can be atomically abrupt, which is great for research on phenomena like interface reactions. By controlling the number of laser pulses, one can grow films from just a few nanometers to several microns. This wide thickness range means PLD can create ultra-thin films for fundamental studies

(e.g. tens of nm to see quantum or strain size effects) or thicker films that can function as actual fuel cell layers (e.g. a 5 μm dense electrolyte). Achieving a 5 μm dense film of LSGM by conventional sintering is possible but may have imperfections; PLD achieved it with high quality and that yielded exceptional cell performance.

The quality and properties of PLD films depend strongly on parameters like substrate temperature, oxygen pressure, laser energy (fluence), and repetition rate. Optimizing these is crucial. Higher substrate temperatures generally promote better crystallinity and epitaxy. For example, growing LSCF or LSGM typically requires substrate temperatures of 600–800 °C to get a crystalline perovskite film [2,18-22]. If grown too cold, films might be amorphous or have secondary phases. However, too high can cause re-evaporation of volatile elements. So, a balance is found experimentally for each material. Oxygen pressure controls oxidation and also plume dynamics. A moderate O_2 pressure (say 100mTorr) will thermalize the ablated species more, leading to a smoother film growth, but if too high, the plume may scatter too much and deposition rate drops. If too low, the film may be oxygen-deficient or have a high density of oxygen vacancies, which can alter conductivity. For instance, YSZ grown in very low pressure might come out oxygen-deficient (and thus slightly reduced, affecting electronic conductivity). Setting the right oxygen pressure ensures films have the desired oxygen content and phase.

The energy per pulse (e.g. J/cm²) influences how much material is ablated. Higher fluence ablates more material (faster growth) but can also produce particulates (from the target). Lower fluence yields smoother films but slower deposition. Optimization aims for stoichiometric ablation without large particulates (which can create defects in the film). Target-substrate distance and angle can affect film uniformity and plume spread. In research setups, substrates are often small (1 cm²), so uniformity is not a big issue, but for larger substrates, one might need to adjust distance or even

raster the laser spot for even ablation. The overall goal of optimization is high-quality crystalline films with desired composition because that generally correlates with better functional properties. For example, a well-optimized PLD LSGM film was dense, single-phase, and smooth, yielding an electrolyte with low area-specific resistance that translated to high cell power. If growth conditions were off (say, wrong oxygen pressure), one could end up with a film with Ga deficiency or second phases, which would hurt performance.

Chapter 2: Experimental

2.1 Study Overview

This study systematically investigates the PLD growth of LSGM and LSCF films by varying deposition parameters. Specifically, films were deposited at three different substrate temperatures and three different oxygen pressures, resulting in a total of nine unique conditions for each material. Throughout the process, critical parameters like laser fluence, annealing time and pressure were kept consistent to isolate the effects of temperature and background oxygen pressure on film properties. Structural characterization was performed on the films to determine film thickness, lattice parameters, and crystallinity.

After analysis of the base 18 samples, an optimal growth condition (temperature and pressure) was selected for subsequent growths. Heterostructures of LSGM and LSCF were grown using the best conditions identified from the single-layer experiments. Additionally, thinner films of LSGM and LSCF were deposited at the optimal parameters to assess how reduced thickness impacts crystallinity, lattice parameter, and deposition rate. By analyzing how deposition conditions influence film characteristics, this study provided insight into the optimization of PLD-grown LSGM and LSCF films to ultimately learn more about the intrinsic properties governing SOFC performance.

2.2 PLD Process Overview

This section details the fabrication procedures for epitaxial growth of LSGM and LSCF films deposited on $SrTiO_3$(STO) using PLD. The quality of the films is highly dependent on the quality of target material, preparation of the substrate, laser settings, and deposition parameters in the PLD chamber. A systematic approach was employed to ensure reproducible film growth to view the

effect of changing deposition parameters on the final quality of the film. The overall experimental process of using PLD consists of several key stages:

Table 1: PLD experimental workflow

Step	Description
Target Fabrication	Production of high-quality LSGM and LSCF targets by pressing and sintering to ensure proper phase and density
Substrate Preparation	Cutting, cleaning, and bonding STO substrates to promote epitaxial growth and secure mounting during deposition
Laser Setup	Adjust laser voltage and measuring spot size to maintain laser fluence within the desired range for consistent ablation
PLD Growth Procedure	Installing targets and substrates, achieving vacuum, setting deposition conditions, and performing thin-film growth

Each step in this process plays an important role in determining film crystallinity, strain state, and electrochemical performance. Optimization of these parameters is essential for developing high quality films, and ultimately high-performance SOFC materials. Understanding the relationships between deposition conditions, film structure and properties will be covered in the following section regarding characterization.

2.2.1 PLD Target Fabrication

Targets for LSGM and LSCF were prepared using commercially purchased powders, following a series of grinding, pressing, and sintering yielded dense and uniform targets suitable for ablation in the PLD chamber.

As-received LSGM and LSCF powders were characterized using powder X-ray Diffraction to verify the base perovskite phase and to compare with the final target at the end of the process. Nine grams of each powder were manually ground using a pestle and mortar to break up agglomerates

into a fine and uniform powder. Grinding continued until the powders exhibited a very smooth texture (approximately 2 hours) to ensure better compaction in pressing steps. To further increase uniformity and decrease particle size, acetone was added to the powder, and wet grinding was performed until the acetone was completely evaporated (approximately 1 hour). This left behind a very finely milled dry powder ready for pressing.

The processed powders were loaded into a cylindrical die for uniaxial pressing. After loading the power into the die set, the die was placed in an MSE Supplies 24T tablet press and slowly pumped to a pressure of 30 Mpa. When the pressure stabilized at 30 Mpa, it was left to dwell for 1-2 minutes before slowly releasing the pressure; these measures were taken to prevent cracking or defects during the pressing and removal process. To further increase pellet density and improve its strength, the pellets were then subjected to cold isostatic pressing (CIP). After carefully removing the target from the die set, it was transferred to a thin latex balloon. A vacuum pump was outfitted with a narrow tube, which was inserted into the balloon. While pinching the balloon around the tube (to prevent air from re-entering), the vacuum pump was turned on to evacuate the internal air. Once sufficient vacuum was achieved, the tube was withdrawn while maintaining the seal by continuous pinching. The balloon was then tied to preserve the vacuum state before placing in the oil chamber of the CIP. After sealing the CIP chamber, it was pumped to 200 Mpa, enhancing the mechanical integrity and density of the target. Following the CIP process, the balloon was removed from the chamber and thoroughly cleaned and dried before removing the target (to prevent oil contamination). The dense targets were then transferred to alumina crucibles for tube furnace sintering.

After the crucibles were placed in the middle of the tube furnace using a copper push rod, a controlled heating profile for both LSGM and LSCF was employed. The heating profile consisted

of a slow ramp-up to the sintering temperature (minimizing thermal shock), then a dwell period, and finally a slow ramp-down back to ambient temperature (to prevent cracking or internal stresses).

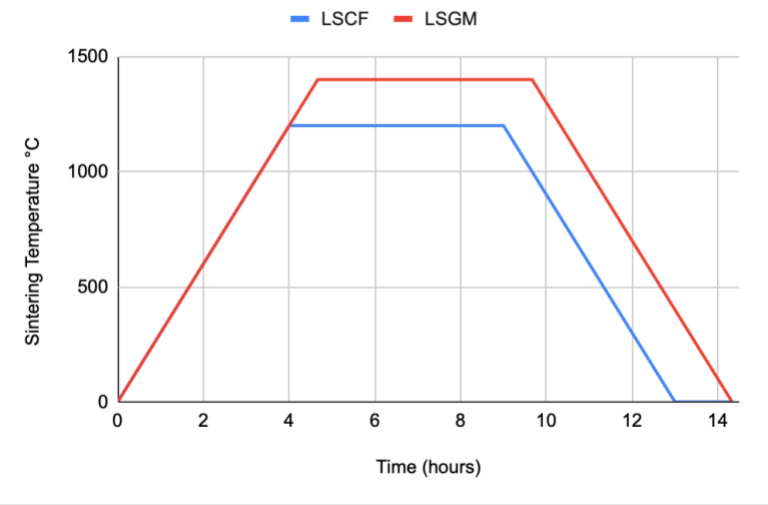

Figure 3: Target sintering profiles

The resulting targets were then characterized using powder x-ray diffraction to verify phase purity before use in PLD. Below are the XRD charts comparing the sintered targets with the received powders. The peaks for both LSGM and LSCF were indexed and matched the expected perovskite phase.

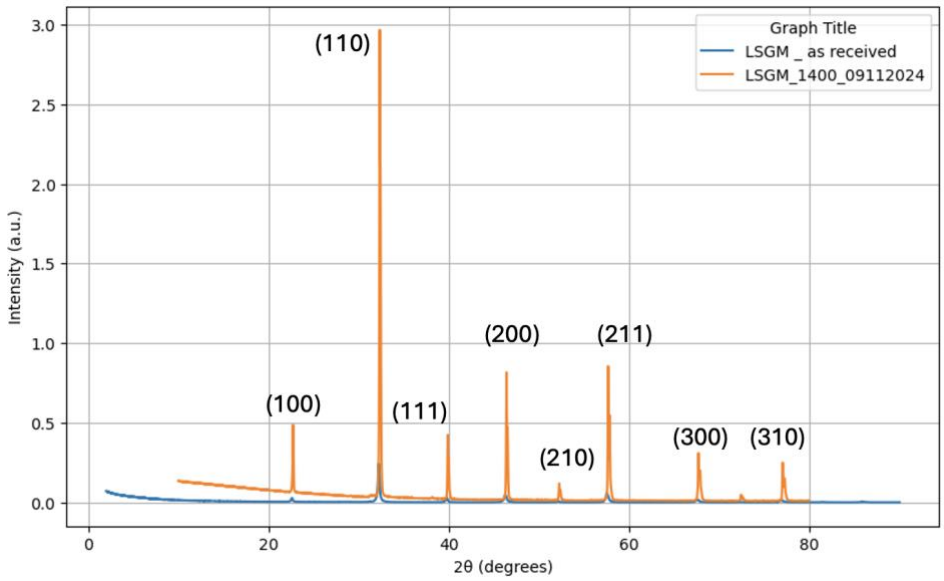

Figure 4: Powder XRD comparison of LSGM target vs powder

The LSGM targets lattice parameter was determined using Nelson-Riley function approximation discussed in section 2.3.2 Lattice Parameter Determination. The bulk lattice parameter was determined to be approximately 3.915 Å, slightly higher than the parent material $LaGaO_3$ of 3.910 Å.

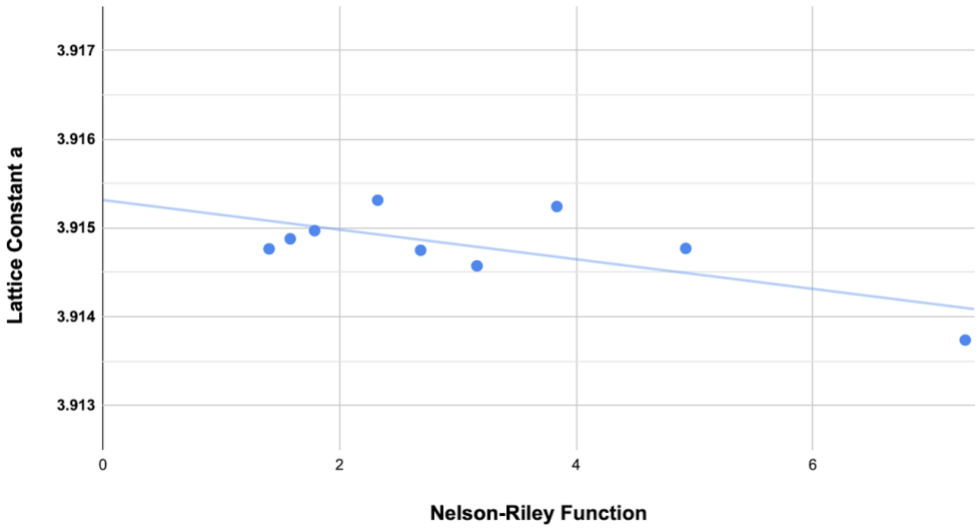

Figure 5: NR approximation of bulk LSGM

Similarly, the LSCF peaks were indexed and compared with the reference powder to verify pure phase.

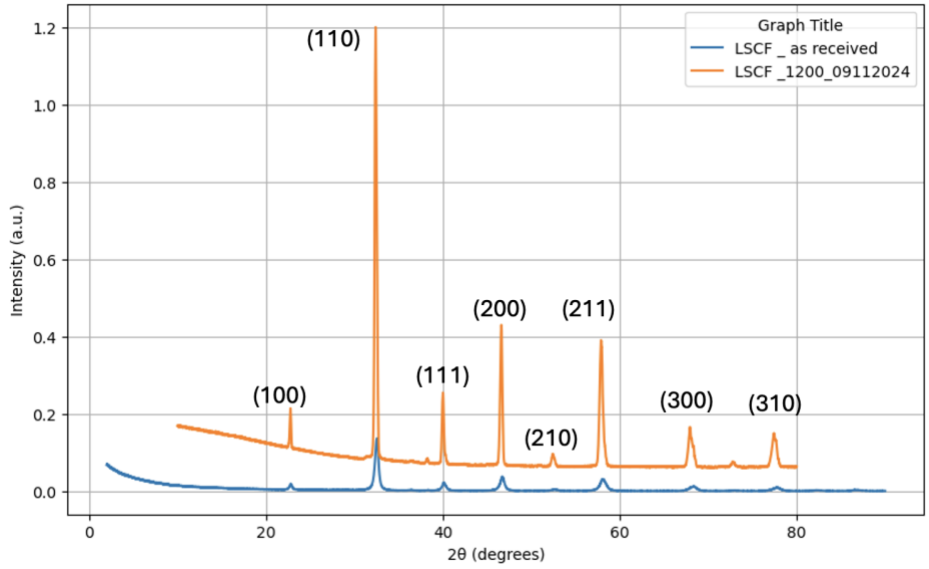

Figure 6: Powder XRD comparison of LSCF target vs powder

The bulk lattice parameter of LSCF was determined to be approximately 3.896 Å, lower than the parent material $LaFeO_3$ of 3.96 Å. To further assess the quality of the sintered targets, optical microscopy was used to inspect the surface morphology. The images reveal that the targets are densely packed with minimal visible porosity, indicating successful compaction and sintering. Such dense targets are critical for PLD, as they help ensure consistent ablation behavior and thus, unform film growth. Below are representative optical microscope images of the targets taken at 5000x magnification.

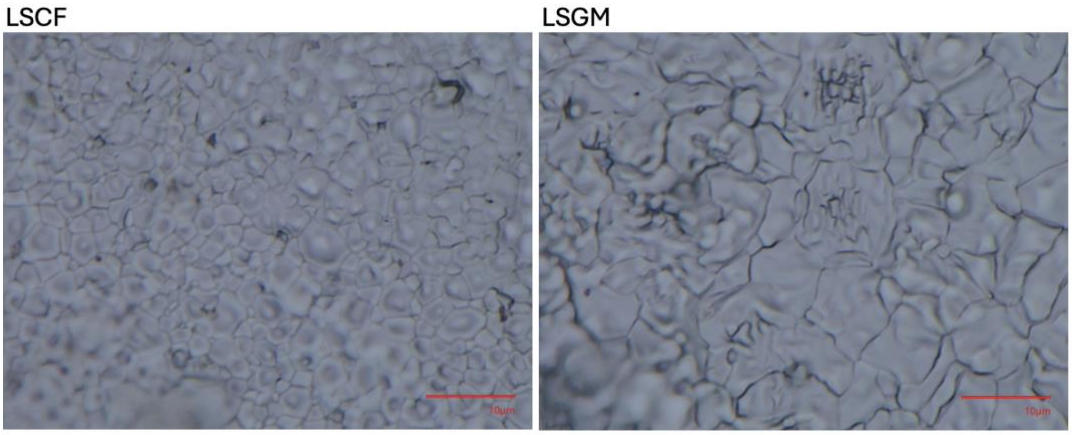

Figure 7:Target surface optical microscope images

2.2.2 Substrate Preparation

Proper substrate preparation is essential for achieving high-quality thin films during PLD. For this study the main substrate used was STO, with one sample of LSGM grown on $LaAlO_3$ due to its nearly mismatched nature with STO. A summary of the substrates can be seen below.

Table 2: Substrate information

Name	**Shinkosha STO Substrate**	**MTI LAO Substrate**
Finish	One Side Polished	One Side Polished
Cut size (Final size)	3mm x 3mm x 1mm	5mm x 5mm x 0.5mm
Orientation	(100)	(100)
Lattice Parameter	3.905Å	3.78Å

First the bulk square 10mm STO substrates were sectioned into square 3mm pieces using a diamond wire saw. This step ensured greater value from using one purchased substrate for nine samples. After the cutting procedure, the substrates were immersed in acetone and placed in a Sonicator for 10-minute increments to ensure all residual glue and dust from the cutting process

was completely removed. The substrates were then dried using a nitrogen stream and placed in storage to prevent contamination.

Before a deposition, the substrate underwent a multi-step ultrasonic cleaning process to remove surface contaminants and ensure a clean surface to grow on. Below are the procedures for both STO and LAO.

Table 3: Substrate cleaning procedures

STO Ultrasonic Cleaning Procedure	LAO Ultrasonic Cleaning Procedure
Acetone - 10 minutes	2% Hellmanex - 5 minutes
Isopropyl Alcohol - 10 minutes	De-ionized water - 5 minutes
De-ionized water - 10 minutes	Acetone - 5 minutes
	Isopropyl Alcohol - 5 minutes
	De-ionized water - 10 minutes

Post-cleaning, the substrates were then bonded to a clean substrate holder plate using a “silver paint” mixture (silver powder dispersed in acetone). After painting a circle of the silver mixture onto the center of the plate, the substrate was placed on top. The mounted substrates were then heated to 170°C via hotplate to evaporate the acetone, leaving behind a stable bond between the substrate and the holder. Once secured, the holder (with the attached substrate) was installed into the PLD chamber.

2.2.3 Laser Setup

Proper calibration of laser energy and fluence is necessary to achieve consistent ablation and stoichiometry transfer of target material to the deposited film. Thus, the setup and tuning of laser energy was critical to ensure consistency between samples. Laser fluence is a measure of the

energy density of the laser at the focal point (target surface). It requires the laser energy before hitting the target and the total area of the laser spot. Below is the equation used to calculate fluence, where E in Joules is the laser energy after entering the PLD chamber, and x and y are the measured dimensions of the spot size.

$$f = \frac{\mathrm{E}}{\mathrm{x} * \mathrm{y}} \quad \left(\frac{\mathrm{J}}{\mathrm{cm}^2}\right)$$

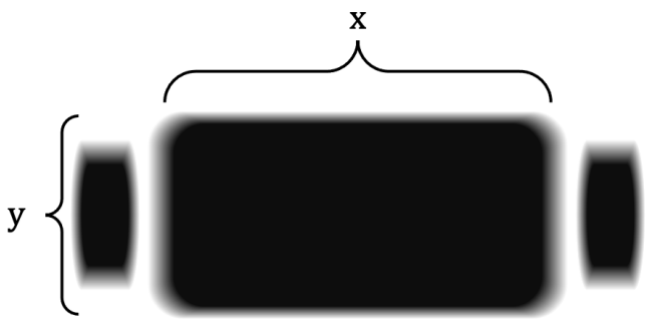

Figure 8: Laser spot size illustration

The laser energy was first checked at a set operating condition of 19kV and 10Hz. Initial measurements were taken after the laser warmup sequence, and directly at the laser shutter. After this, the energy was measured after passing through all optics, immediately before entering the PLD chamber window (accounting for losses due to optical reflections and scattering). Loss through the PLD chamber window was approximated to be ~15%. This final adjusted value was recorded as the final laser energy (within the chamber) and was used in the fluence calculation. To assess the laser spot size, the laser was set to fire at 1 Hz, and thermal paper (laser testing paper) was placed at the target level. A single pulse was used to create a visible mark, and the dimensions of the spot were measured using digital calipers. These dimensions were used to calculate the laser fluence. The target fluence range for depositions was maintained between 2.95 and 3.4 J/cm^2 to ensure consistent target ablation across experiments. If the measured fluence was outside the

desired range, adjustments were made by varying the laser voltage accordingly. Once the new voltage was set, the calibration process was repeated to verify that the adjusted fluence fell within the specified range.

2.2.4 PLD Growth Procedure

The deposition of LSGM and LSCF films was carried out using PLD under controlled temperature, pressure, and laser fluence conditions. The growth process involves substrate and target installation, chamber evacuation, heating, O_2 introduction, deposition, and annealing.

The PLD process began by securing the prepared substrate holder plate inside the deposition chamber. The target material, either LSGM or LSCF, was affixed to a target holder using double-sided tape to ensure stability during ablation. Proper target alignment was verified by confirming that the laser spot was centered on the target. If misalignment was observed, optical components were adjusted accordingly. This step also served as an opportunity to measure the laser spot size, as described in the laser setup section.

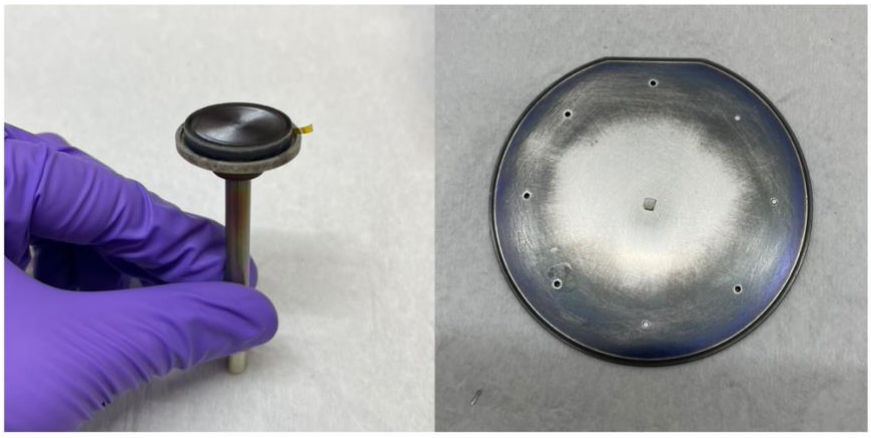

Figure 9: Mounted target (left) and mounted substrate (right)

With the target and substrate in place, the target rastering angles were set to ensure that the laser spot moved across both edges of the target during rotation. The target rotation speed was then

adjusted to promote even ablation and reduce localized target degradation. Similarly, the substrate rotation speed was set to ensure even film deposition.

Before initiating the evacuation process, the chamber door was cleaned with isopropyl alcohol (IPA), dried, and securely sealed. The vacuum pump was then powered on, and the necessary valves were opened to begin chamber evacuation. The turbo pump speed was set to 1000 Hz, and the system was pumped down until a base pressure on the order of 10^{-6} Torr was achieved. The maximum achieved vacuum was recorded before proceeding. Once an adequate vacuum was established, the heater controller was programmed with a ramp profile to bring the system to the desired deposition temperature.

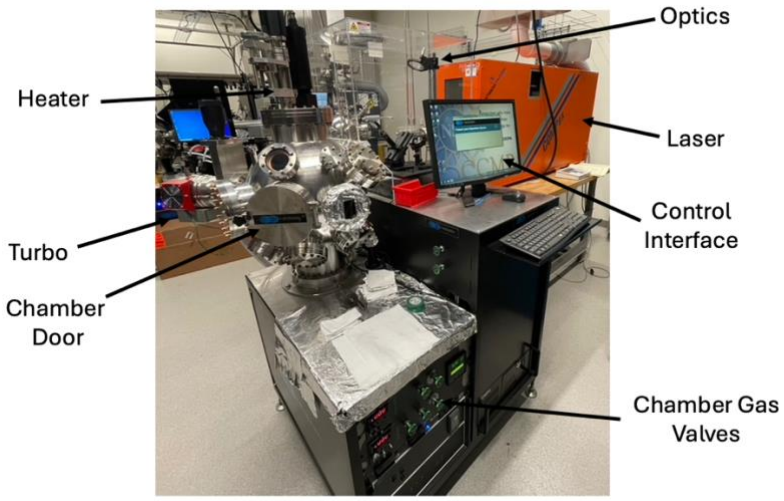

Figure 10:PLD component breakdown

With the system at the deposition temperature, the oxygen pressure was introduced to maintain controlled growth conditions. First, the turbo pump speed was reduced to 200 Hz to allow controlled gas introduction. The mass flow controller (MFC) was used to manually regulate the oxygen flow rate (in standard cubic centimeters per minute, sccm) until the desired deposition

pressure was reached. This process required iterative adjustments to stabilize the pressure before proceeding.

Once the deposition conditions were stabilized, the laser shutter was opened, and the laser was activated using the calibrated settings as discussed in the laser setup section. The total deposition time was determined based on the number of laser pulses and pulse frequency. For example, the base 18 deposition experiments were conducted with 30,000 laser shots at a frequency of 10 Hz, corresponding to a deposition time of 3,000 seconds (50 minutes).

Upon completion of the deposition, the laser was turned off, and the target rotation, target rastering, and substrate rotation were deactivated. The vacuum pump and MFC were also shut off, and all valves were closed to seal the chamber.

Following deposition, an annealing step was performed to optimize film properties. The heater controller was reprogrammed with a post-deposition heating profile, where the substrate was held at the deposition temperature for 1 hour before being gradually cooled to ambient temperature. Annealing was conducted at a pressure of 150 Torr for all samples, which was achieved by introducing oxygen through a coarse valve. The valve was then closed, and the heating profile was initiated.

After the annealing process was completed, the chamber was vented with nitrogen to bring it back to atmospheric pressure. The heater was raised, and the chamber door was opened to remove the substrate holder plate. The deposited film was carefully detached from the plate by applying shear force using a flat crystal edge against the substrate. Finally, the sample was stored in a nitrogen-purged desiccator cabinet to prevent atmospheric contamination before characterization.

2.3 Characterization

Following thin-film deposition, a set of characterization techniques were employed to evaluate the structural and electrical properties of the LSGM and LSCF films. Accurate characterization is essential to find a correlation between deposition parameters and resulting structure of the film. Ensuring that the grown films exhibit the desired crystallinity, phase purity, thickness and electrical properties will ultimately push closer to the goal of uncovering the inherent properties of these material systems.

X-ray Diffraction (XRD) was utilized to determine the crystal structure, phase composition, and epitaxial quality of the films. From the XRD data, lattice parameters were extracted to assess the mismatch between layers, as well as the deviation from bulk properties. Film thickness was also extracted from XRD data through analysis using Laue Oscillations, and verification using X-ray reflectivity (XRR). The resulting film thicknesses provide insight into the deposition rate of materials given the different growth parameters. Electrical properties of LSCF were characterized using the four-prober (van der Pauw) method to determine sheet resistivity and other properties allowing for a broad assessment of the conductivity variations as a function of changing deposition conditions.

These characterization techniques collectively provide an understanding of the structural and functional aspects of the films' enabling further refinement of deposition parameters to optimize these materials for SOFC applications.

2.3.1 X-Ray Diffraction

X-ray diffraction (XRD) was used to characterize the crystalline structure, phase composition, and epitaxial quality of the LSGM and LSCF targets and films. XRD operates on the principle of

constructive interference of scattered X-rays from atomic planes in the crystal lattice. This relationship can be summarized by Bragg's Law:

$$n\lambda = 2dsin\theta$$

where n is an integer order of wavelength λ, d is the interplanar spacing of crystal lattice planes, and θ is the incident angle of the wave [23]. When the path difference between the scattered wave from a set of planes is an integer multiple of the wavelength, then constructive interference occurs, producing a high intensity diffraction peak that can be measured by a detector.

In this study, multiple XRD measurements were conducted to assess the different aspects of film quality and structural properties, including $\theta - 2\theta$ scans, $2\theta - \omega$ scans, rocking curves (ω scans), and reciprocal space mapping (RSM).

Before thin film analysis, $\theta - 2\theta$ scans were conducted on the LSGM and LSCF powders as received, and after sintering in the target fabrication process. This was done to ensure perovskite structure and purity. In this scan, the incident beam and detector angel are coupled ensuring that only diffraction from lattice planes parallel to the sample surface is detected. For powder samples, this measurement yields a diffraction pattern representing randomly oriented crystallites. Sharp, well-defined peaks indicate high crystallinity, while peak broadening may suggest small grain size. This initial characterization step was essential in confirming that the targets used for PLD were pure LSGM and LSCF perovskite phase before proceeding to thin film growth.

A $2\theta - \omega$ scan was performed on each sample to determine the crystal structure and phase purity of the deposited films. In this configuration, the incident X-ray angle ω and detector angle 2θ maintain a constant relationship throughout the scan [23]. This allows measurement of diffracted peaks corresponding to lattice planes parallel to the substrate surface. The position of the peaks

indicated interplanar spacing which can then be used to determine lattice parameters of the material [23]. The intensity and peak width provide insight into the degree of crystallinity and crystallite size. By comparing the diffraction peaks with reference data, secondary phases or preferential orientations can be identified. Comparing the diffraction peaks with other samples at varying growth conditions can provide insight into how different temperatures and pressures impact the structure and quality of the deposited film. Similar to the base $2\theta - \omega$ scan, X-ray reflectivity (XRR) allows for film thickness approximation through curve fitting (using software) or using oscillation period equations. Functionally, XRR is performed like the $2\theta - \omega$ scan, but with very small incident angles.

To assess crystalline quality, the rocking curve was performed. In a rocking curve measurement, the detector is fixed at a specific 2θ position corresponding to a specific Bragg reflection peak (lattice plane), while the incident angle ω is changed. The width of the rocking curve peak provides valuable information about the crystalline quality, suggesting how well-aligned these crystal planes are. For example, a broad full width at half maximum (FWHM) could suggest increased dislocation density or strain variations within the film [23]. In growing epitaxial films, the rocking curve is critical for determining how ordered the film is, and its degree of alignment between the film and substrate.

RSM was performed to obtain a more detailed characterization of strain in the films. RSM involves measuring intensity in both 2θ and ω directions creating a two-dimensional map of reciprocal lattice points. This essential takes multiple $2\theta - \omega$ scans varying both quantities around a specific reflection peak like 103. RSM can provide insights on whether the film is fully strained, partially relaxed, or completely relaxed. One can also extract the in-plane and out-of-plane lattice constants,

to determine the degree of epitaxial strain, however this analysis could not be completed due to time constraints.

By utilizing these techniques, the structural properties of LSGM and LSCF were analyzed, allowing for the correlation of growth parameters on lattice constants and crystallinity.

2.3.2 Lattice Parameter Determination

The lattice parameter of the deposited films was determined using the data collected from $2\theta - \omega$ scans and Bragg's Law. First, Bragg's Law can be rearranged to solve for the interplanar spacing d:

$$d_{hkl} = \frac{n\lambda}{2sin\theta}$$

where the diffraction order n is taken as 1, λ is the X-ray wavelength from the emitter, and θ is the observed peak angle. If peak positions were ambiguous due to peak broadening or overlapping peaks, a combination of Voigt and Gaussian functions was used to approximate the peak position by fitting the diffraction peaks. This was achieved using common python packages, numpy, pandas, matplotlib, scipy, and a specialty package lmfit. Lmfit is a tool that extends optimization methods from scipy that minimizes least-squares for non-linear curve-fitting of a dataset.

Once peak positions have been noted for each set of Miller indices (hkl) they were related to the lattice parameter a by:

$$a = d_{hkl} * \sqrt{h^2 + k^2 + l^2}$$

To further refine the determination of the lattice parameter, a Nelson-Riley function was used. The Nelson-Riley function is expressed as:

$$F(\theta) = \frac{1}{2}\left(\frac{\cos^2\theta}{sin\theta} + \frac{\cos^2\theta}{\theta}\right)$$

A linear fit was applied to a plot of the calculated lattice parameters against the Nelson-Riley function, and the intercept of this line corresponding to $F(\theta) = 0$, provides the most accurate estimate of the lattice parameter [24].

2.3.3 Film Thickness Determination

Film thickness was estimated using multiple X-ray based techniques, selected based on the specific features observed in the XRD data of each sample.

For films exhibiting a distinct film and substrate peaks, a variation of Bragg's Law was applied to determine an approximate film thickness. In cases where Laue Oscillations were present, film thickness was approximated using the spacing between oscillation peaks. A similar method was used for analysis of XRR data that showed oscillations.

Starting from Bragg's Law, the film and substrate interplanar spacings and corresponding angles are separated.

$$n\lambda = 2d_S sin\theta_S$$

$$n\lambda = 2d_f sin\theta_f$$

In these equations, d_s and θ_s correspond to the substrate, and d_f and θ_f correspond to the film. For small-strain approximations, film thickness can be approximated using the following equation:

$$d_f = d_s\left(1 + \frac{1}{t}\right)$$

Which can then be substituted into Bragg's law for the film.

$$\lambda = 2d_s\left(1+\frac{1}{t}\right)\sin\theta_f$$

Interplanar spacing of the substrate can be solved for independently resulting in the equation for d_{hkl} shown at the beginning of section 2.3.2. Next, d_s is substituted back into the equation.

$$\lambda = 2\left(\frac{n\lambda}{2sin\theta_s}\right)\left(1+\frac{1}{t}\right)\sin\theta_f$$

For films with nearly mismatched substrates, a small-angle approximation can be used to simplify the equation.

$$sin\theta_f \approx sin\theta_s + (\theta_f - \theta_s)cos\theta_s$$

After rearranging, and solving for *t* yields the final equation:

$$t = \frac{\lambda}{2(\theta_f - \theta_s)tan\theta_s}$$

It is important to note that the underlying assumptions used to employ this equation add to the error of the calculation. Specifically, the small strain assumption and small angle approximation make this equation more accurate in thin films (<100nm) with nearly mismatched lattice parameters. The average mismatch for LSGM and LSCF on STO substrate are below 1%, meeting that criterion, however many of the films are likely thicker than 100nm leading to error in this calculation.

To approximate the film thickness using Laue Oscillations, the following equation was used:

$$t = \frac{\lambda}{\Delta\theta cos\theta_f}$$

where $\Delta\theta$ corresponds to the angular difference between consecutive Laue oscillations in the $2\theta - \omega$ scan, and θ_f corresponds to the main film peak angle [25].

2.3.4 Nanometrics Electrical Characterization

Electrical characterization of the LSCF films was performed using a Nanometrics Hall measurements system, employing the Van der Pauw method for resistivity and Hall effect analysis. This technique allows for accurate determination of sheet resistivity and carrier properties of samples connected to four electrical contacts.

For measurements, the magnetic field strength was set to 0.51 T. A constant current source was configured to deliver current in the milliamp range, while the voltage was limited to 200mV, with a built in delay of three seconds to improve measurement stability and signal averaging. The LSCF sample was first placed in the sample holder, ensuring the four-probe contacts were aligned with the corners of the sample. After verifying the contact between the four probes, the measurement sequence was started. The system provides sheet resistivity as the primary measurement, along with the Hall coefficient, carrier mobility, and sheet carrier density.

Following the initial set of measurements, low-resistance indium contacts were soldered to the corners of the samples to improve electrical contact quality and reduce contact resistance. The same measurement procedure was then repeated with the indium contacts in place.

Chapter 3: Results and Discussion

3.1 Process Optimization for Bi-Layer Growth

To successfully grow high-quality heterostructures, it was first necessary to determine the optimal deposition conditions for individual LSGM and LSCF films. This process was guided by structural characterization using XRD, providing insights into the lattice parameters at various growth conditions, as well as film crystallinity and quality. Optimizing these parameters is crucial not only for achieving high-quality heterostructure growth but also for understanding the intrinsic properties of single-crystal LSGM and LSCF.

One of the main challenges in optimizing LSGM growth was distinguishing its XRD signature from that of the STO substrate, as their lattice parameters are closely matched. Across the base set of nine growth conditions, films grown at 800°C and 150mTorr exhibited the most distinct LSGM peak, indicating successful film growth.

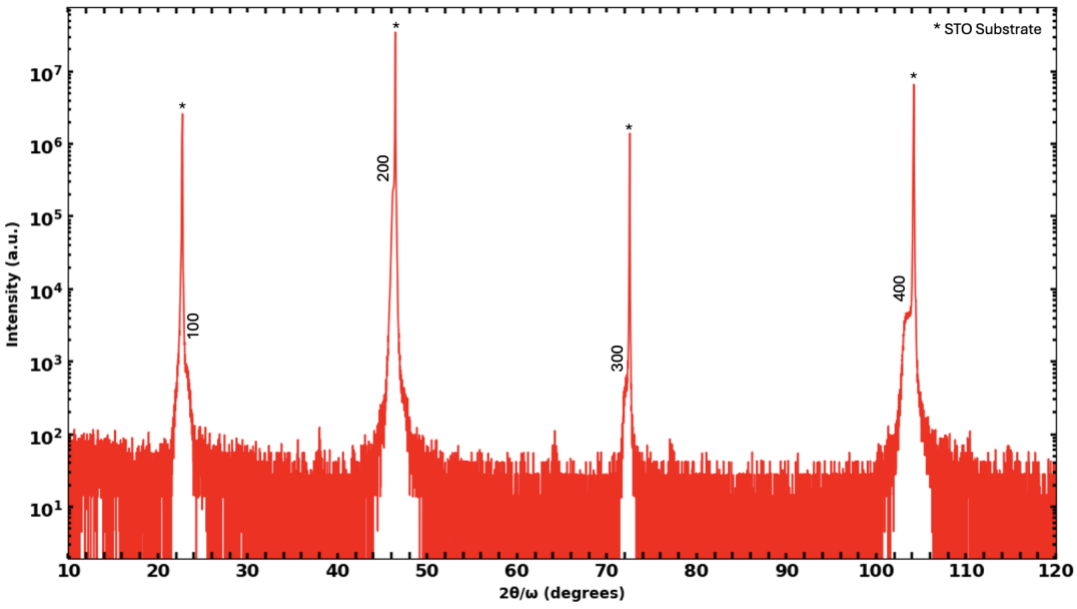

Figure 11: XRD scan for LSGM film grown at the optimized condition

The graph above shows the $2\theta - \omega$ scan of single crystal LSGM peaks as clear shoulders to the STO peaks. At other growth conditions little evidence of growth could be found either as a result of very close matching of STO lattice parameter, or lack of film growth.

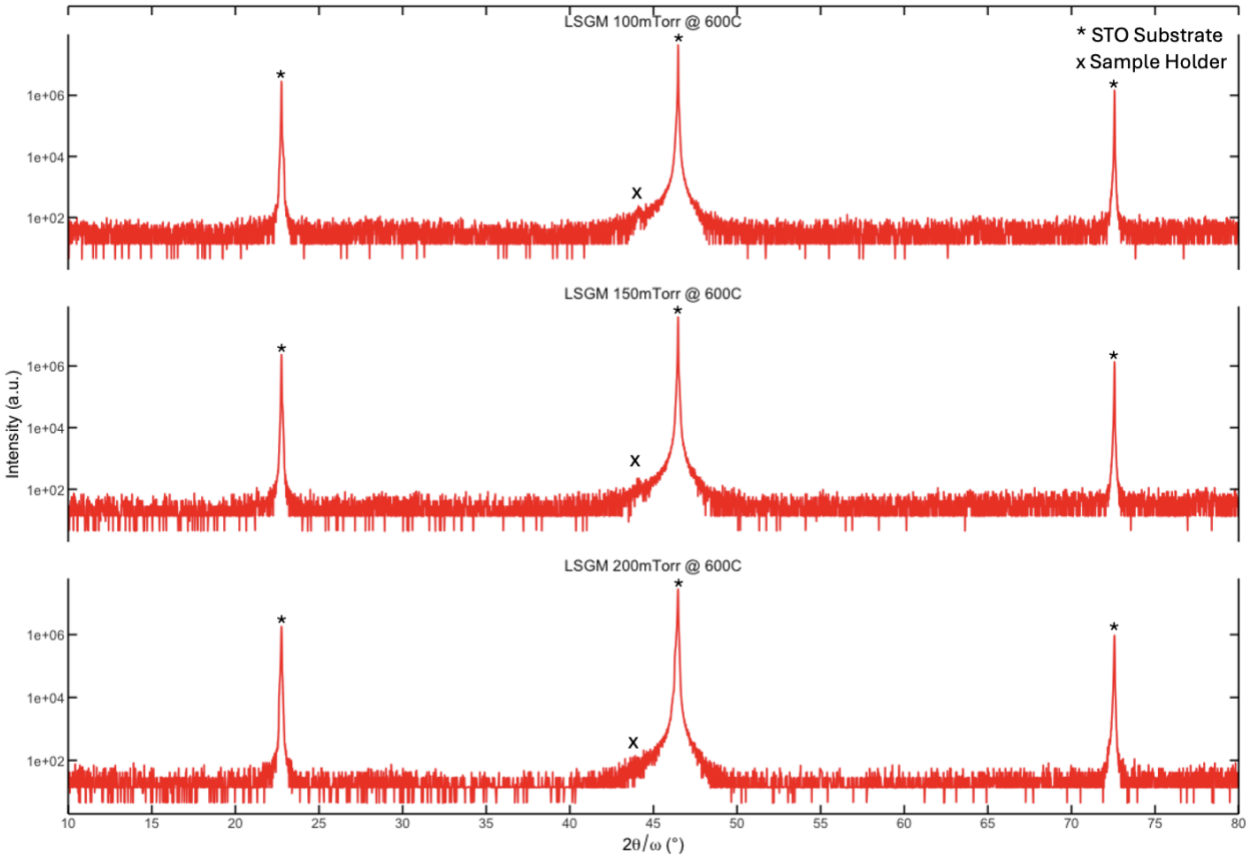

Figure 12: XRD scans of LSGM films grown at 600°C

In the 600°C regime at various pressures, no apparent growth occurred apart from slight peak broadening in the 200mTorr sample. In contrast, at 800°C, broad peaks of LSGM can be seen in all samples, with very clear components visible in the 150mTorr sample, indicating high quality single crystal growth.

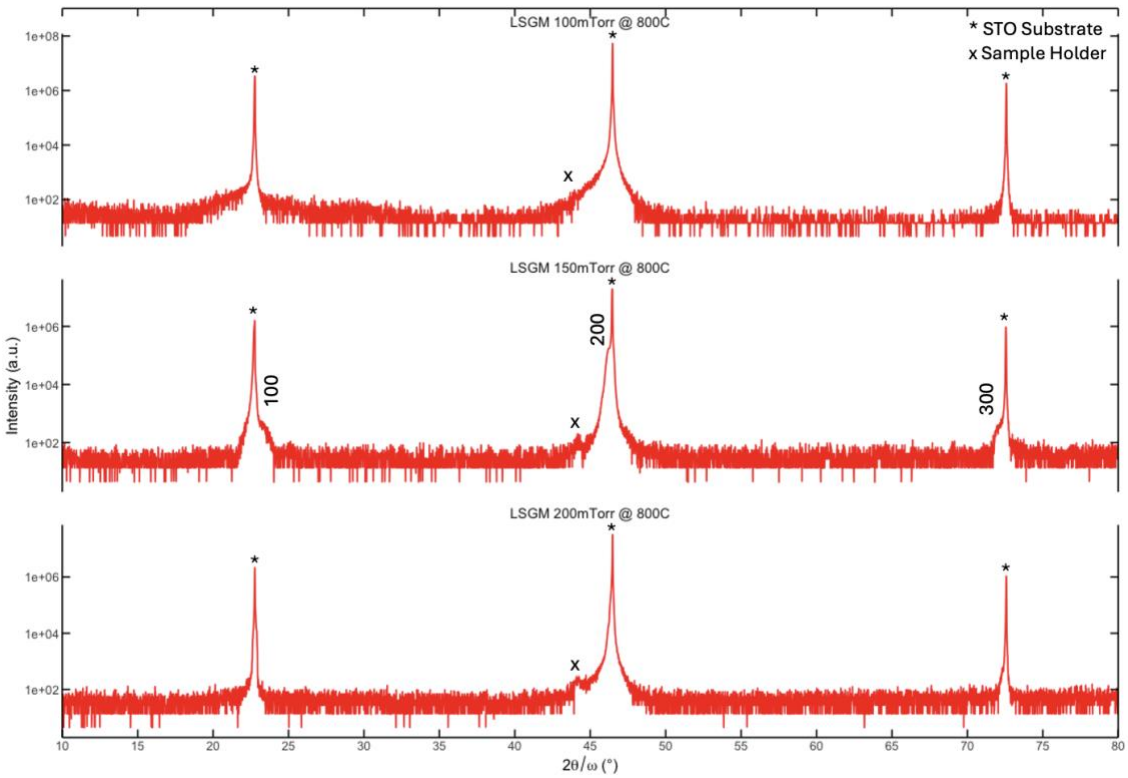

Figure 13: XRD scans of LSGM films grown at 800°C

Rocking curve scans about the 200 and 400 plane reflections show the film peaks in comparison to STO peaks.

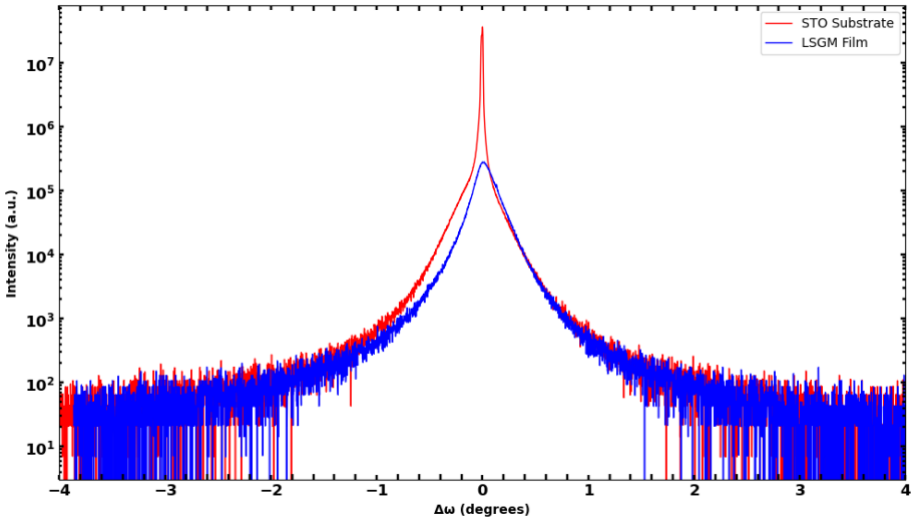

Figure 14: LSGM RC of 200 plane at optimal growth conditions

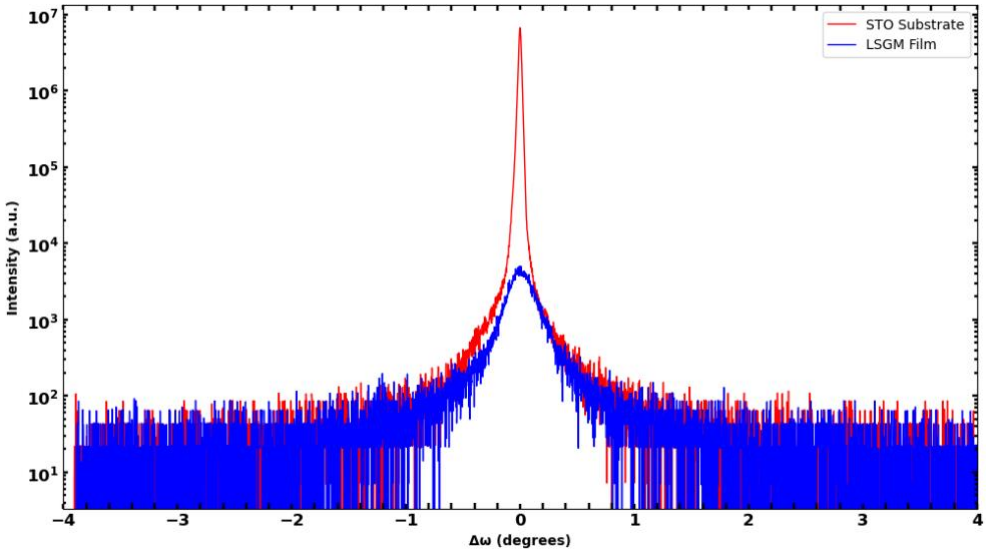

Figure 15: LSGM RC of 400 plane at optimal growth conditions

High film quality can be concluded from these rocking curve plots, as the FWHM of the 200 plane was calculated as 0.169° and 400 plane as 0.181°. For these reasons, out of the nine sets of growth conditions, 800°C at 150mTorr was selected as the optimal growth condition to proceed with heterostructure growth.

Unlike LSGM, LSCF exhibited a more noticeable mismatch with the STO substrate, leading to film peaks in all XRD scans (some sharp and some broad). To further evaluate the film quality, the rocking curves and Laue oscillations were analyzed. Narrower rocking curve FWHM values indicated higher crystal quality, while Laue oscillations confirmed this along with smooth interfaces. The optimized LSCF growth conditions were determined to be 800°C at 150mTorr, as this combination yielded sharp peaks, and very well-defined Laue oscillations.

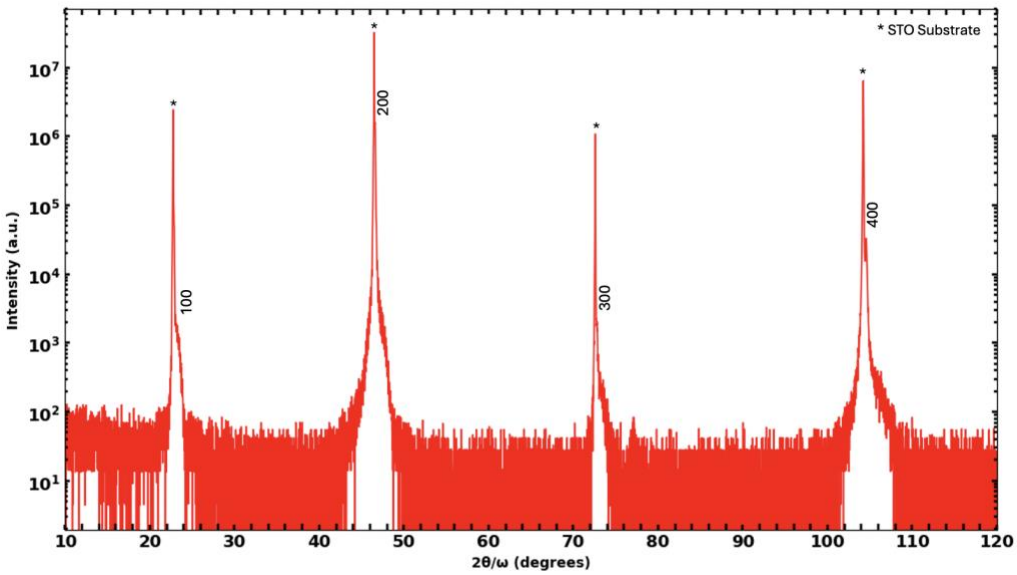

Figure 16: XRD scan for LSCF film grown at the optimized condition

More detail, and clear Laue oscillations can be seen in a detailed view of the 200-plane reflection region.

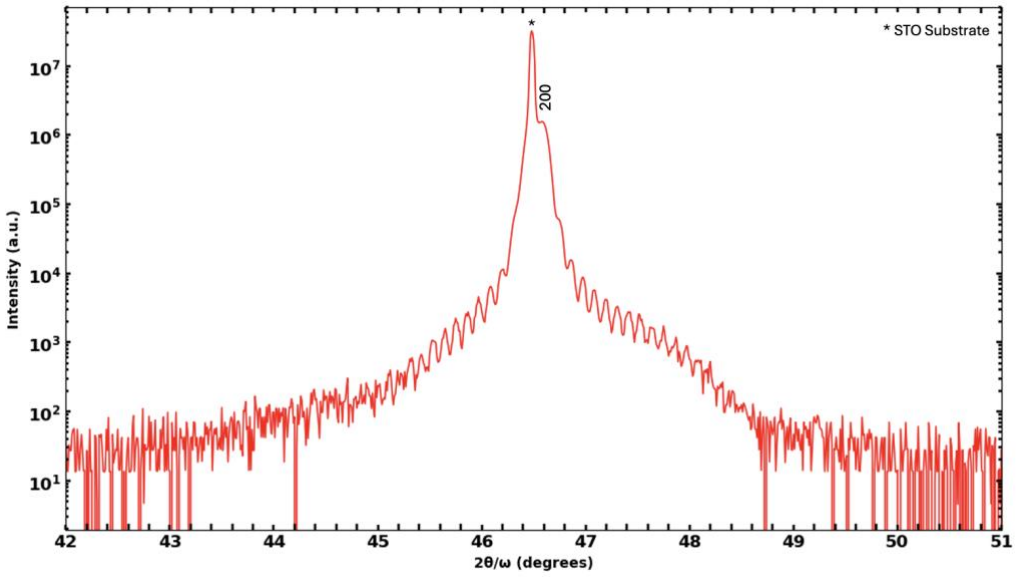

Figure 17: XRD 200 detailed scan for LSCF film grown at the optimized condition

Rocking curve analysis of this LSCF film, also showed a high degree of crystallinity as the FWHM about the 200 plane was 0.072°, and around the 400 was 0.0977°.

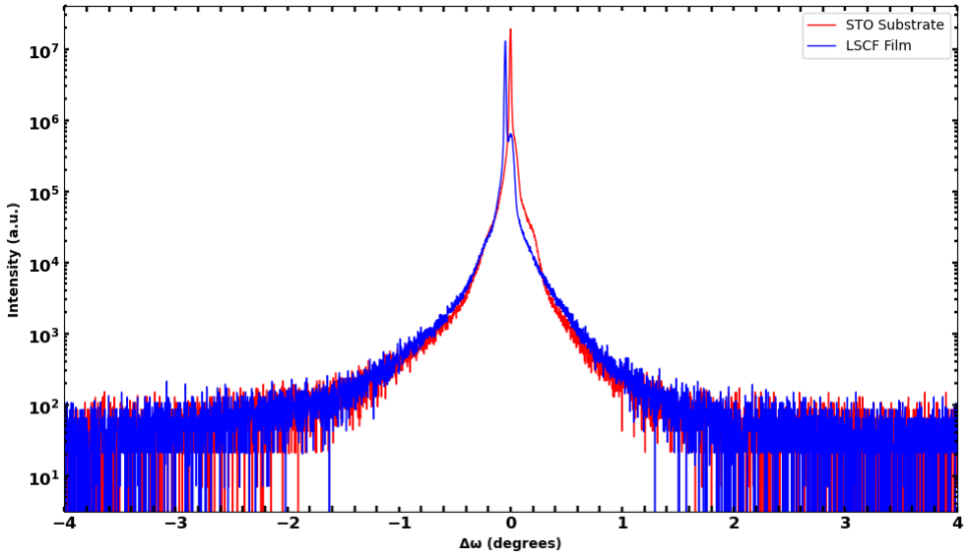

Figure 18: LSCF RC of 200 plane at optimal growth conditions

The FWHM about 200 plane was approximated by first subtracting the region of the substrate peak, and using gaussian fitted data to fill the void. Then the FWHM was calculated based on the width at half maximum intensity of the film peak (right side raw data and left side fitted data).

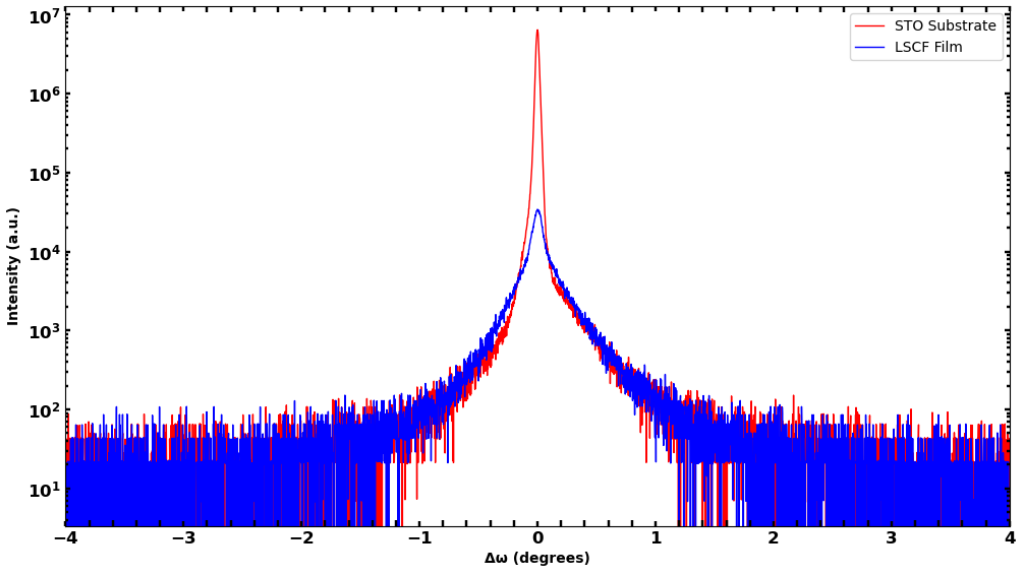

Figure 19: LSCF RC of 400 plane at optimal growth conditions

Using the optimized deposition conditions, heterostructures were fabricated with the following layer sequence: 1. STO substrate, 2. LSCF, 3. LSGM. The XRD analysis confirmed the presence

of both LSGM and LSCF layers, though peak broadening of the LSCF layer suggested possible interdiffusion at the LSCF/LSGM interface.

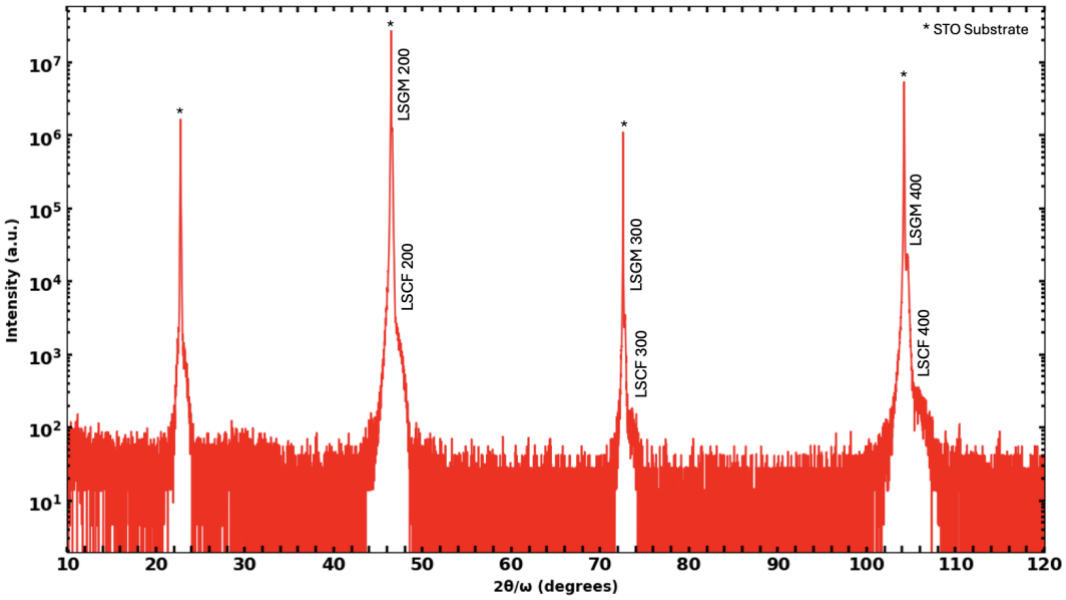

Figure 20: XRD scan for LSCF LSGM Heterostructure at the optimized condition

Further analysis of the 200 and 400 plane rocking curves of the heterostructure indicated a degradation in LSCF crystal quality, potentially due to diffusion at the interface.

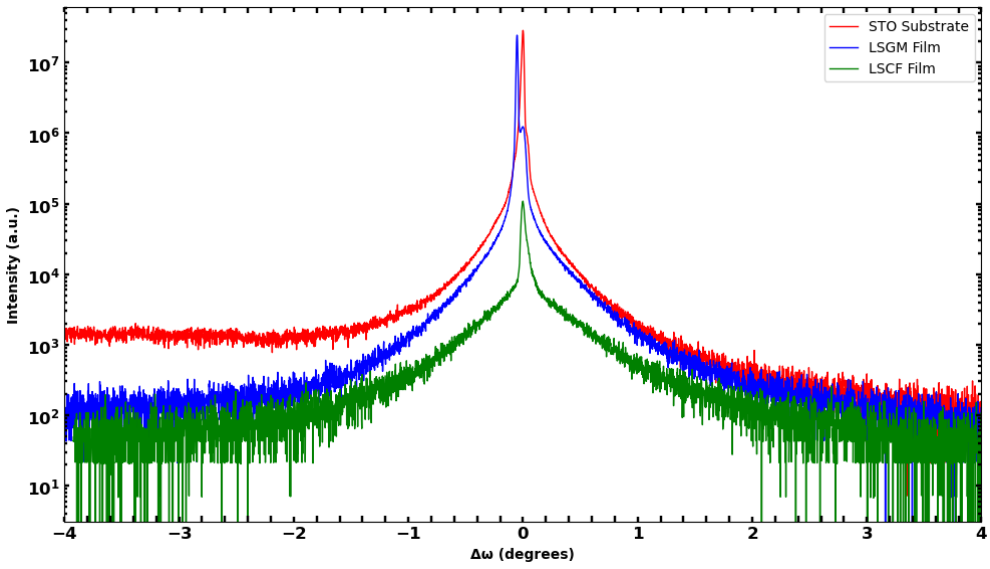

Figure 21: Heterostructure RC of 200 plane at optimal growth conditions

RC analysis of 200 plane revealed an LSGM FWHM of 0.066° with substrate peak subtraction, and an LSCF FWHM of 0.05°. Analysis of the 400 plane revealed an LSGM FWHM of 0.0918°, and an LSCF FWHM of 0.696°.

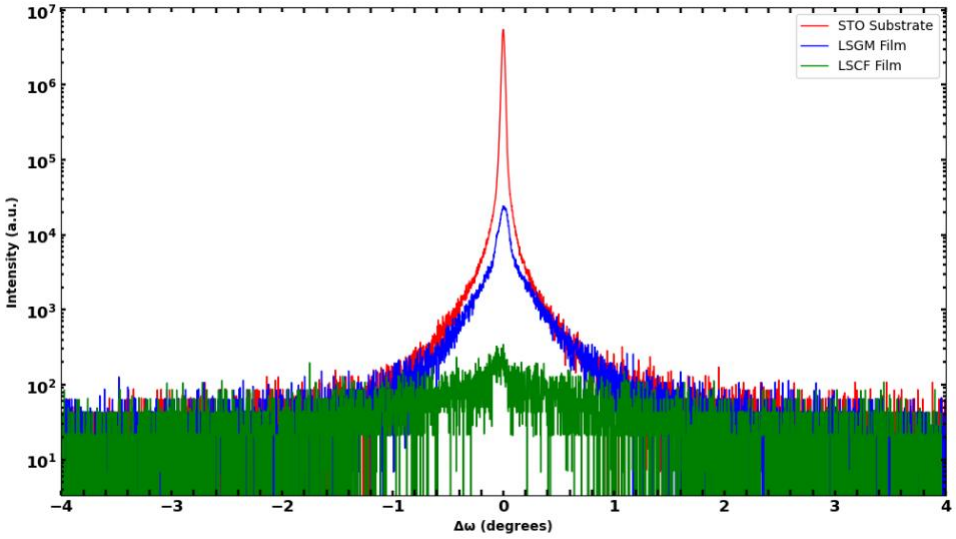

Figure 22: Heterostructure RC of 400 plane at optimal growth conditions

To mitigate potential diffusion at the interface, a heterostructure was grown at a reduced temperature of 700°C while maintaining 150mTorr.

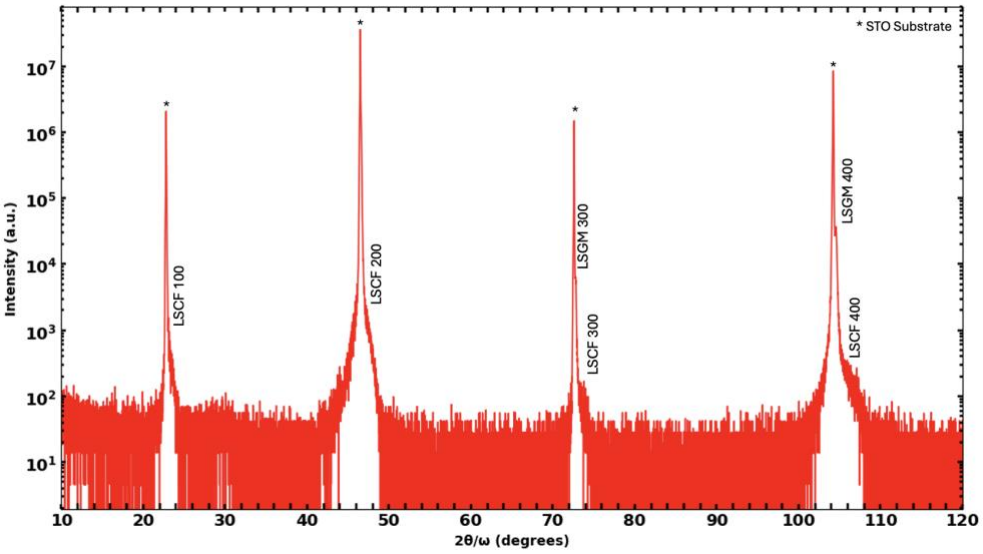

Figure 23: XRD scan for LSCF LSGM Heterostructure at reduced temperature

While this adjustment showed some structural differences, definitive conclusions regarding interfacial quality require further characterization beyond XRD. Additional techniques, such as cross-sectional transmission electron microscopy (TEM) and elemental mapping, will be necessary to assess the extent of interdiffusion and its impact on structural properties.

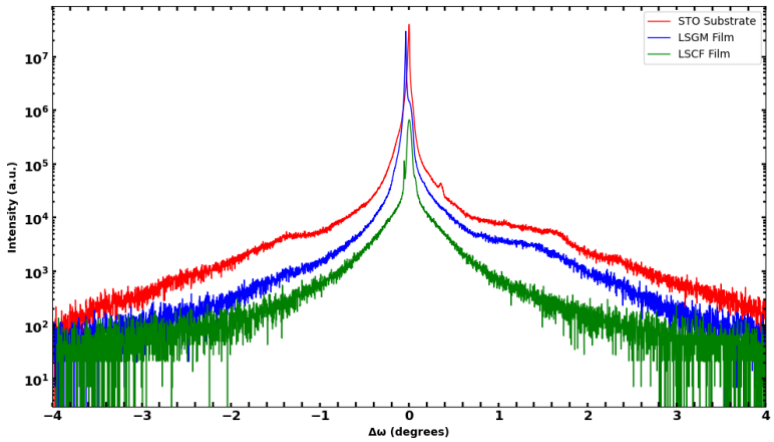

Figure 24: Heterostructure RC of 200 plane at reduced temperature

RC analysis of 200 plane revealed an LSGM FWHM of 0.078° with substrate peak subtraction, and an LSCF FWHM of 0.0434°. Analysis of the 400 plane revealed an LSGM FWHM of 0.0922°, and an LSCF FWHM of 0.744°.

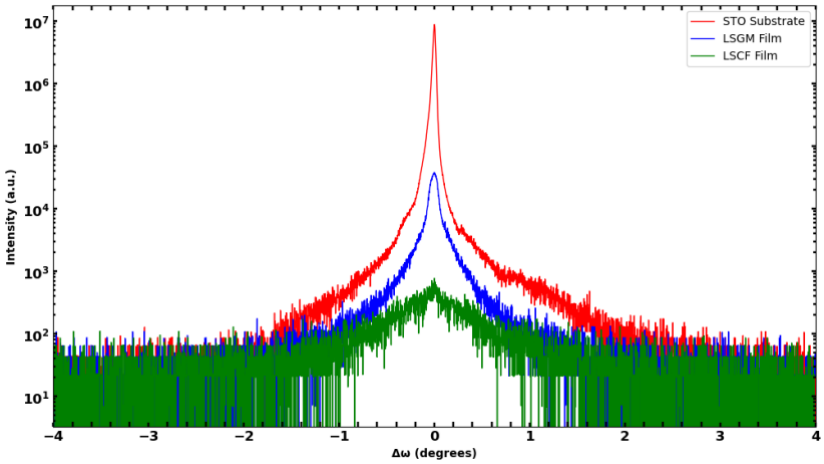

Figure 25: Heterostructure RC of 400 plane at reduced temperature

This section establishes the optimized parameters for individual LSGM and LSCF films and provides an initial assessment of heterostructure growth. However, further studies are required to refine the interface quality and fully understand its impact for functional properties.

3.2 XRD and Structural Analysis

3.2.1 Lattice Parameter Analysis

Following deposition, XRD was used to extract detailed structural information about the grown films. The primary focus of this analysis was the evaluation of the out-of-plane lattice parameter across different growth conditions, providing insight into film deviation from bulk values.

Lattice parameters were calculated from $2\theta - \omega$ scans, with peak positions refined using Voigt and gaussian fitting when necessary. For improved accuracy, the Nelson-Riley method was used to extrapolate the "true" lattice parameter by fitting a line to interplanar spacing measurements as discussed in the experimental section.

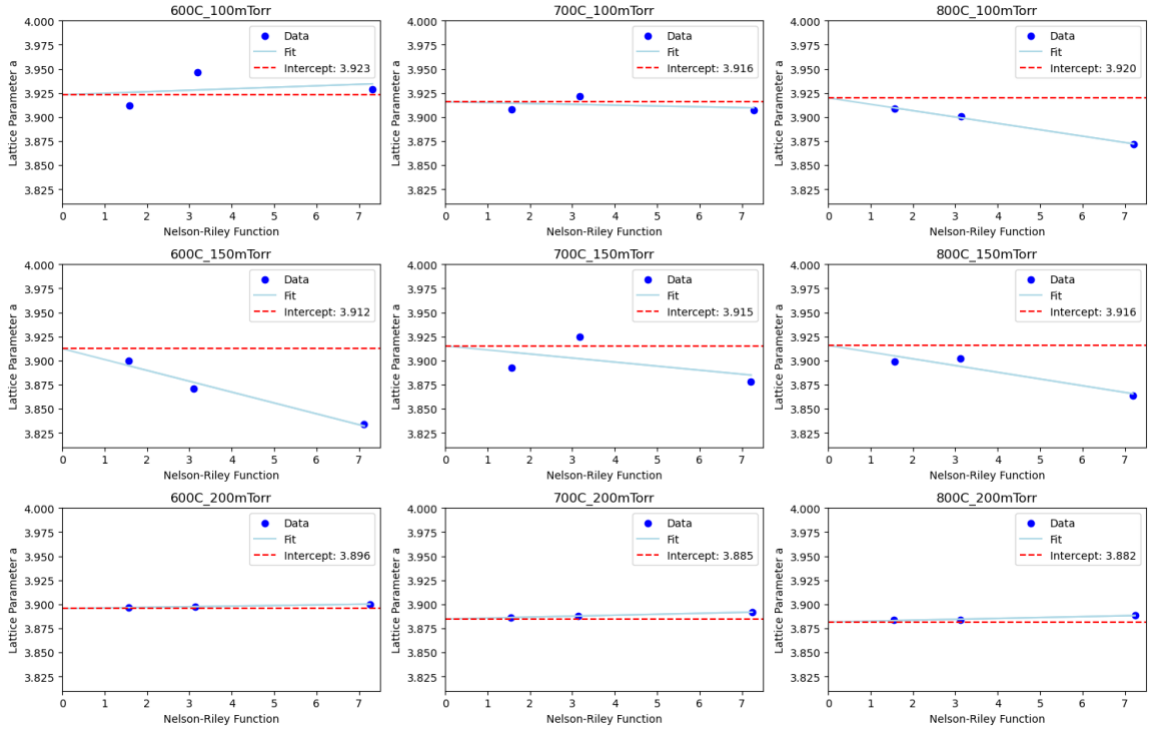

Figure 26: LSCF Nelson-Riley lattice parameter approximation

Across the base growth conditions, a consistent trend emerged for LSCF films. For a given growth temperature, lattice parameter decreases with increasing pressure. In the LSCF system, pressure has a larger impact on the lattice parameter than growth temperature likely due to the role of oxygen vacancies in the lattice.

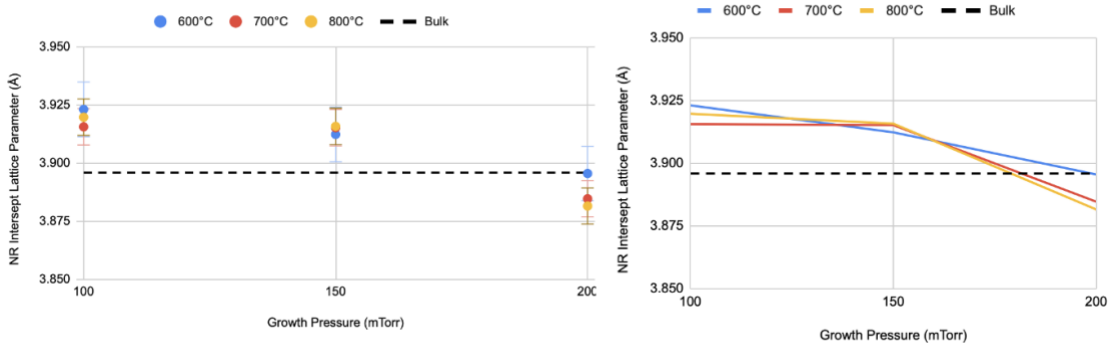

Figure 27: LSCF lattice parameter vs growth pressure

Lattice parameter values at a given pressure are closely grouped regardless of growth temperature and generally stay grouped at the three growth temperatures.

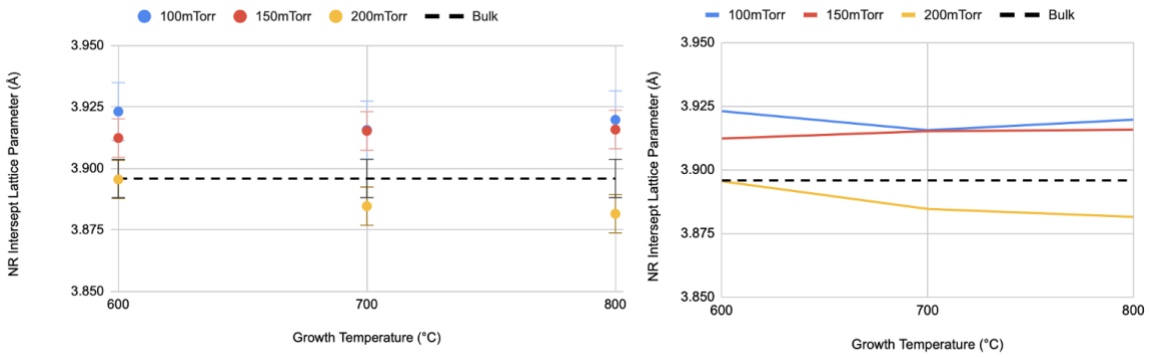

Figure 28: LSCF lattice parameter vs growth temperature

Below is a table summary of the calculated lattice parameters from base LSCF growths along with uncertainty from the calculation and NR approximation.

Table 4: LSCF lattice parameter summary

Growth Condition	600°C	700°C	800°C
200mTorr	3.896 ± 0.002	3.885 ± 0.003	3.882 ± 0.003
150mTorr	3.912 ± 0.033	3.915 ± 0.0239	3.916 ± 0.021
100mTorr	3.923 ± 0.017	3.916 ± 0.008	3.920 ± 0.019

Now a table of mismatch between LSCF film and the STO substrate can be constructed, noting that mismatch at low pressure is the most tensile, and at high pressure is the most compressive.

Table 5: LSCF lattice mismatch summary

Growth Condition	600°C	700°C	800°C

200mTorr	0.243% Compressive	0.524% Compressive	0.604% Compressive
150mTorr	0.188% Tensile	0.261% Tensile	0.276% Tensile
100mTorr	0.461% Tensile	0.271% Tensile	0.376% Tensile

The shifting from tensile to compressive strain indicates that the film strain can be modulated through careful control of oxygen pressure. Understanding and controlling this mismatch is crucial, as it opens the door to strain engineering. This can aid in forming the relationship between targeted strain states, and material properties like conductivity, ionic mobility, and catalytic activity. These insights will be especially valuable in future studies aiming to correlate strain with functional performance and guide design improvements of SOFC components.

Determination of the LSGM lattice parameter was more difficult due to the fact that many of the base growths did not show distinct film peaks. However, many of the heterostructures has unique LSCF and LSGM film peaks, so the LSGM lattice parameter can was determined using those samples along with the best LSGM sample. One sample of LSGM was grown on LAO substrate at the best condition to help determine the fully relaxed lattice parameter. Below is a summary of the NR function interpolated lattice parameters compared to the bulk value found from the target.

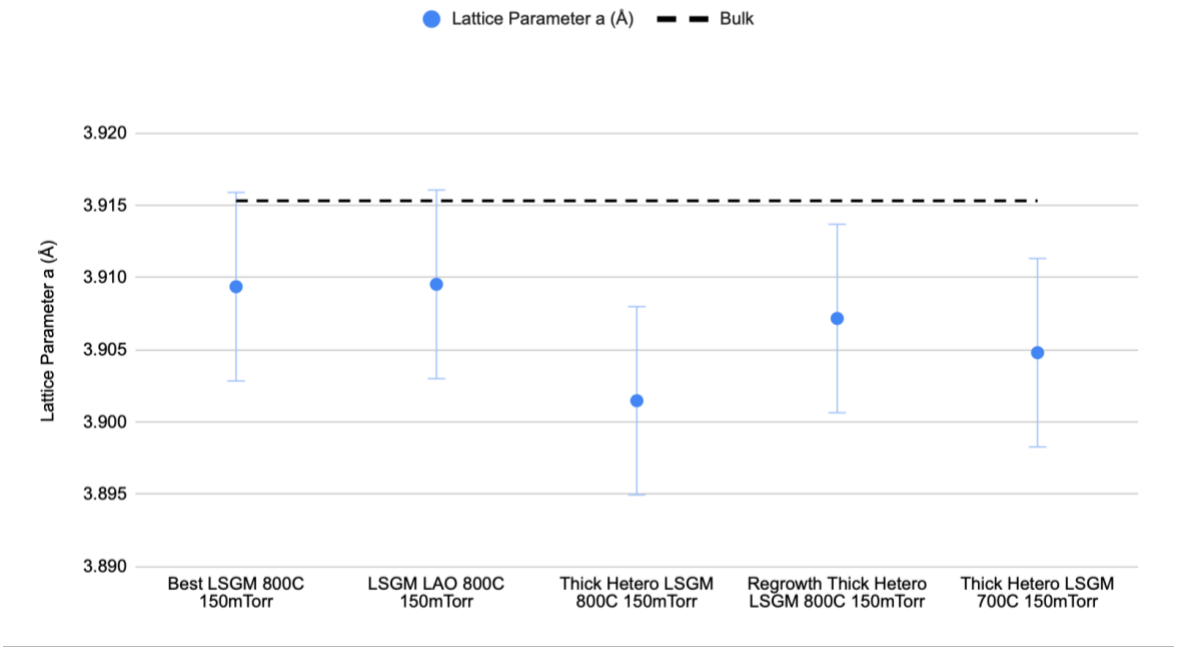

Figure 29: LSCF lattice parameter vs sample

The base LSGM and LSGM on LAO samples show lattice parameters comparable to the bulk, where the heterostructure parameters are slightly lower potentially remaining slightly strained from the LSCF layer below it.

Table 6: LSGM lattice parameter summary

Sample	Lattice Parameter a (Å)
Best LSGM - 800°C 150mTorr	3.909 ± 0.017
LSGM on LAO - 800°C 150mTorr	3.909 ± 0.0042
Heterostructure LSGM - 800°C 150mTorr	3.901 ± 0.012
Regrowth Heterostructure LSGM - 800°C 150mTorr	3.907 ± 0.018
Heterostructure LSGM - 700°C 150mTorr	3.905 ± 0.014

While the full set of LSGM base samples did not consistently yield clearly resolvable film peaks, accurate lattice parameters were successfully extracted from the above samples.

3.2.2 Thickness and Deposition Rate Analysis

The thickness of each LSCF film was estimated using the techniques in section 2.3.3. The calculated thicknesses for each sample are plotted below, showing the value for Laue and Bragg method.

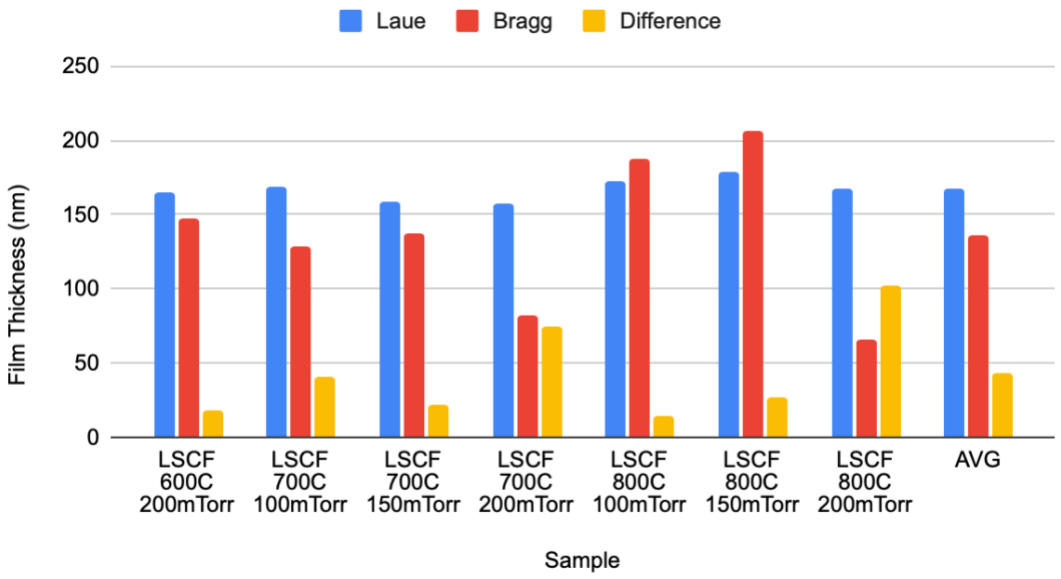

Figure 30: LSCF thickness summary

To better compare film growth across samples, deposition rates were determined by dividing the film thickness by the total number of shots (30,000 shots). These values are summarized in the table below, providing insight into the efficiency of deposition under each set of parameters.

Table 7: LSCF deposition rate summary

Growth Condition	600°C	700°C	800°C
200mTorr	0.0520 Å/shot	0.0400 Å/shot	0.0391 Å/shot
150mTorr	NA	0.0493 Å/shot	0.0641 Å/shot

100mTorr	NA	0.0496 Å/shot	0.0599 Å/shot

These measurements allow for a quantitative assessment of film thickness, and confirm that despite differences in growth conditions, the deposition rate remained relatively consistent across all LSCF samples with an average of **0.05 Å/shot**. It is likely that the target quality, laser fluence, and laser repetition rate have a greater impact on film deposition rate.

Although base samples of LSGM showed little film peak distinction, Bragg's method was employed on the best sample to determine an average deposition rate of **0.065 Å/shot.** Knowing deposition rate is particularly valuable, as it enables future thin-film growths to achieve precise thicknesses for different applications or characterization needs.

3.2.3 RSM Analysis

Reciprocal space mapping was conducted around the (103) reflection to further investigate the structural characteristics and lattice relationships of the best LSGM and LSCF films, as well as the heterostructures grown under optimal and modified conditions. These measurements provide insights into the crystallographic alignment, strain states, and coherence of the growth films relative to the STO substrate.

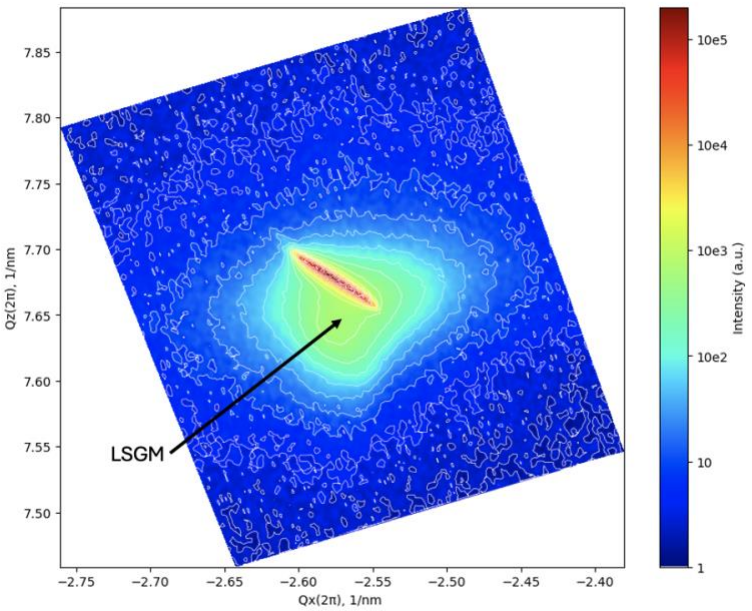

Figure 31: RSM of optimized LSGM

In the figure above, the RSM of the optimized LSGM sample is shown. The highest intensity corresponds to the STO substrate, while a broad LSGM component appears below the STO signal, indicating a lattice with partial relaxation and slight misalignment. This broad LSGM peak is reflected in the FWHM value of the film.

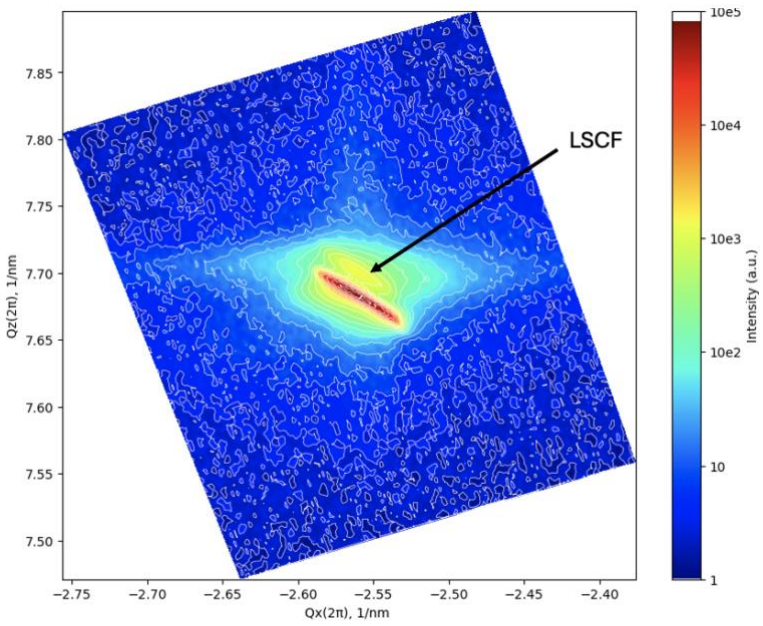

Figure 32: RSM of optimized LSCF

The optimized LSCF sample shows a clear and distinct component above the STO signal, representing the LSCF layer. The sharper signal compared to LSGM suggests better crystalline quality and possible coherency with the substrate.

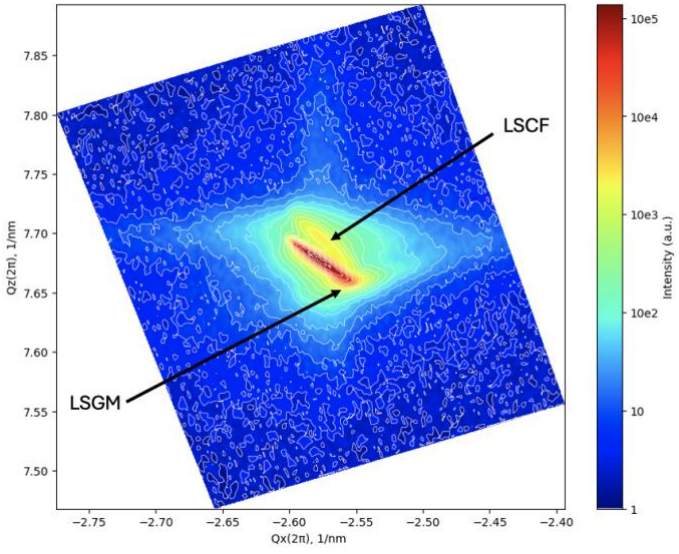

Figure 33: RSM of optimized heterostructure at 800°C

The figure above represents the RSM of the heterostructure grown using the optimized parameters. Here, both a clear LSCF component above the STO peak and an LSGM component below it are visible. These features align with the individual single-film RSMs, confirming successful bilayer deposition and preservation of individual film characteristics. The FWHM of LSGM film, improved in heterostructure growth also visualized in the tighter RSM peak when compared to the single layer growth sample.

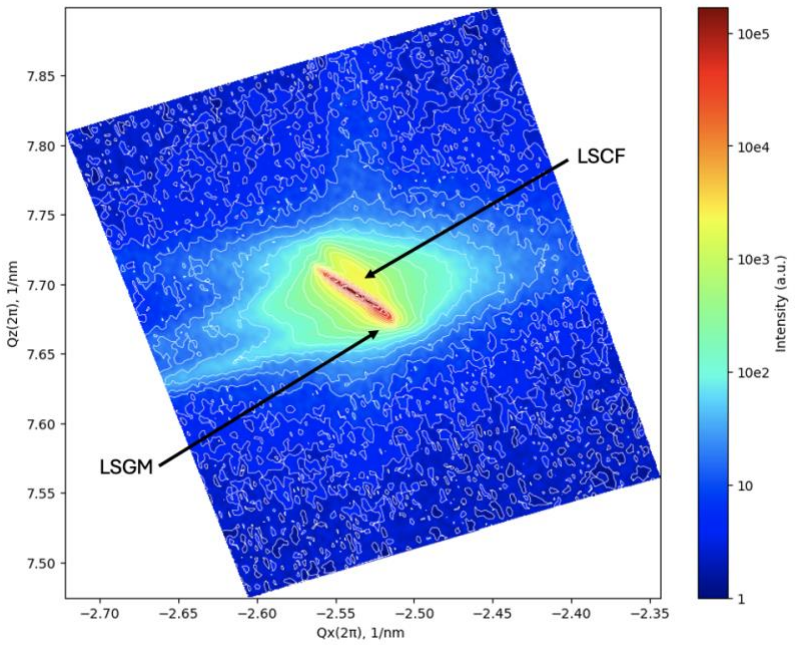

Figure 34: RSM of heterostructure at 700°C

Lastly, the RSM of the heterostructure grown at reduced temperature of 700°C shows similar features to the 800°C sample with subtle differences in LSGM component shape. This could be related to film crystallinity changes due to less interface diffusion however more analysis is needed.

While this initial RSM analysis provides useful insights, father work can be done to extract in-plane and out-of-plane lattice parameters to quantitatively assess strain. Additionally, repeating

RSM analysis on thinner films may reveal more nuanced strain behaviors and guide future strain engineering approaches for tuning material properties.

3.3 LSCF Electrical Characterization

The electrical characterization results for LSCF revealed mixed outcomes. While Hall coefficient, sheet carrier density, and carrier mobility were successfully measured, these values were inconsistent across samples and did not exhibit any clear or reproducible trends. Despite using both raw surface contact and indium soldered contacts to improved reliability, the variability persisted preventing any definitive conclusions regarding carrier transport mechanisms.

In contrast, sheet resistivity exhibited a more coherent trend. For both contact types, resistivity was observed to decrease with increasing oxygen growth pressure, with minimal dependance on growth temperature. These results are shown in the plots below:

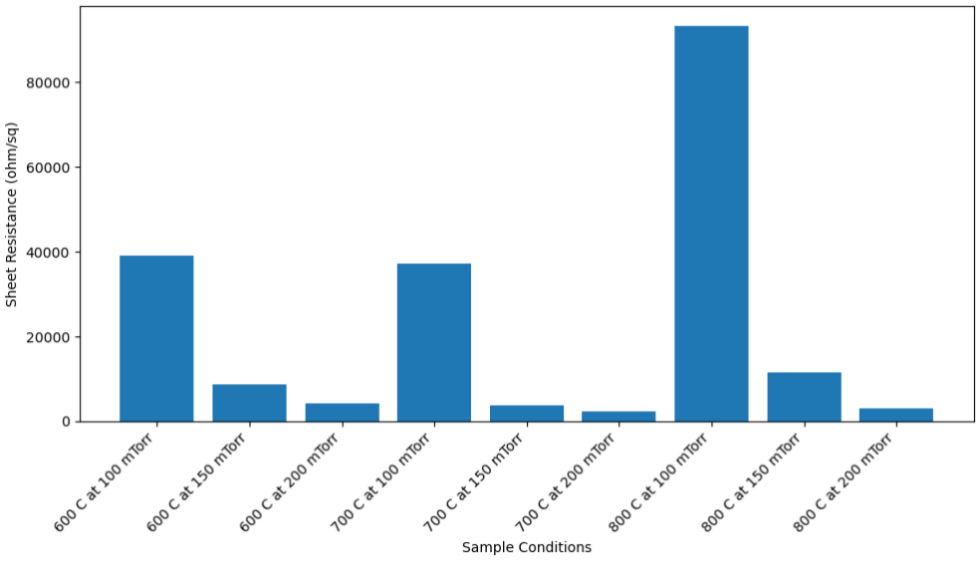

Figure 35: Raw contact sheet resistivity of LSCF vs growth condition

Note that in the indium contact data values for 800°C at 150mTorr are missing, in order to keep the film surface clean for RSM and other future characterization using that sample (at optimal conditions).

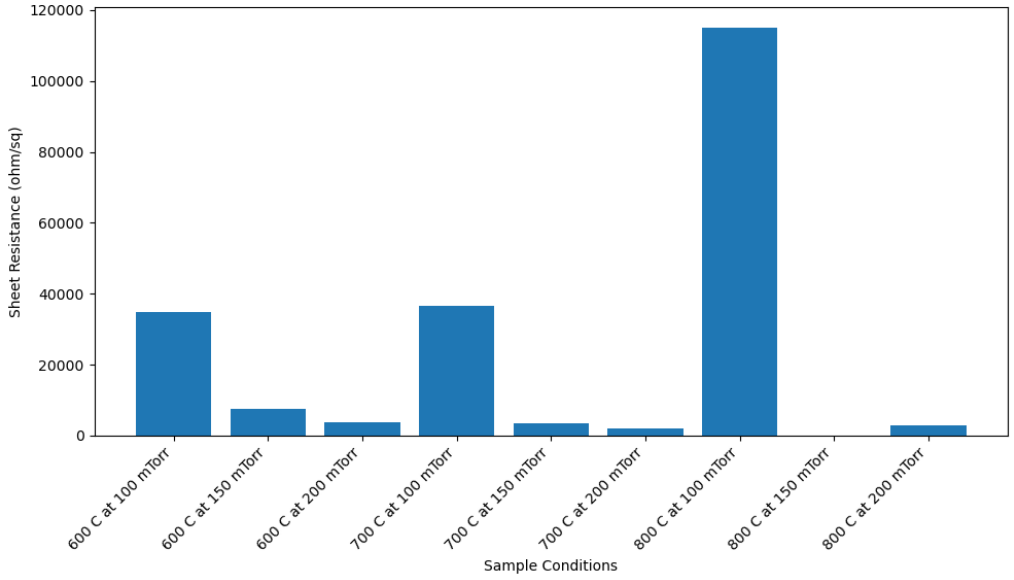

Figure 36: Indium contact sheet resistivity of LSCF vs growth condition

The inverse relationship between oxygen pressure and resistivity may be attributed to improved oxygen incorporation at higher pressure. As oxygen vacancies are filled, electronic conductivity increases due to enhanced carrier mobility and reduced defect scattering. Given LSCF's role as a mixed conductor, this result aligns with expectations for conductivity behavior under varying oxygen stoichiometries. While these parameters did not yield definitive trends, the full set of raw measurements is presented below to illustrate the variability and support future analysis.

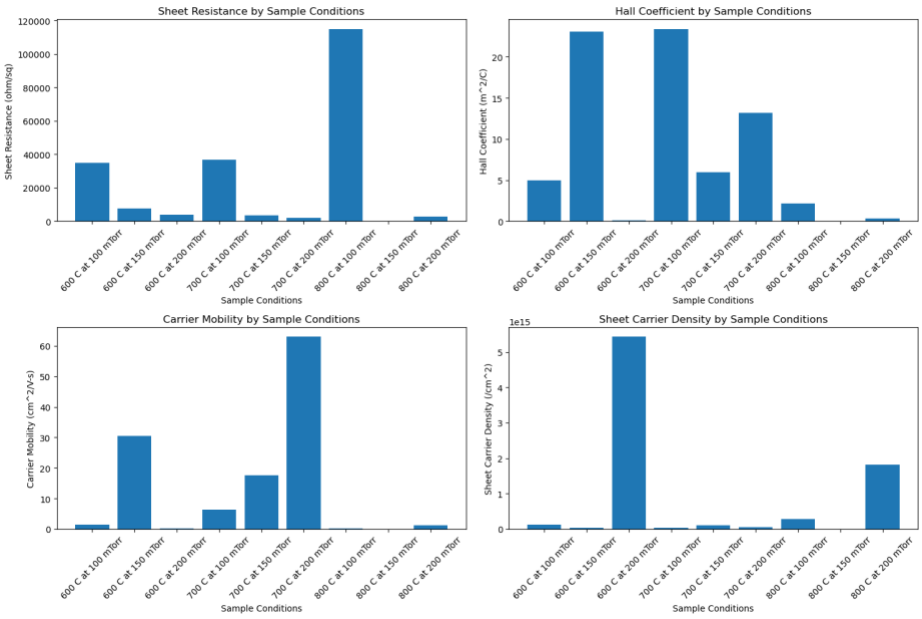

Figure 37: LSCF indium contact data summary

While Hall-based data remain inconclusive, the sheet resistivity measurements provide a useful window into the effects of growth conditions on the film's electronic transport properties.

Chapter 4: Conclusions and Future Work

4.1 Conclusions on SOFC Fabrication using PLD

This study explored the growth and characterization of epitaxial LSGM and LSCF thin films using pulsed laser deposition under systematically varied temperature and pressure conditions. Through analysis of X-ray diffraction patterns, lattice parameter calculations, and electrical measurements, optimized growth conditions were identified for both materials. In particular, LSGM films grown at 800 °C and 150 mTorr exhibited the clearest structural signatures despite the close lattice match with the STO substrate. For LSCF, distinct film peaks were observed across several conditions, with film quality further evaluated using rocking curves and Laue oscillations.

These optimized parameters were subsequently applied to heterostructure growth, enabling the fabrication of bilayer LSGM/LSCF structures. Structural analysis, including reciprocal space mapping and rocking curves, suggested potential interfacial effects such as diffusion or strain coupling, motivating further temperature tuning. A follow-up growth at reduced temperature demonstrated the feasibility of fine-tuning process conditions to address such interface-related challenges.

Electrical characterization of LSCF films showed a consistent trend of decreasing sheet resistivity with increasing oxygen pressure, likely due to vacancy filling. Other electrical parameters exhibited high variability and were ultimately inconclusive under the current experimental setup.

Overall, this work establishes a reproducible framework for the growth of high-quality single-layer and bilayer oxide thin films and provides insight into the interplay between deposition conditions, structural quality, and electrical behavior in epitaxial LSGM and LSCF systems.

4.2 Recommendations for Future Work

While this study has established baseline growth parameters and structural trends for LSGM and LSCF thin films, further investigation is essential to fully understand their intrinsic properties and functional behavior. In particular, future work should prioritize advanced characterization techniques to directly probe the ionic conductivity of these materials. Since LSGM is a well-known ionic conductor and LSCF exhibits mixed ionic-electronic conductivity, characterizing these properties in epitaxial thin films is critical for evaluating their performance in solid oxide fuel cell architectures and related applications.

Electrochemical impedance spectroscopy (EIS) should be employed to measure ionic conductivity and distinguish it from electronic contributions. These measurements, especially when performed across a range of temperatures and oxygen partial pressures, would provide critical insights into defect chemistry, oxygen vacancy dynamics, and conduction mechanisms unique to the thin film form.

Additionally, further structural and chemical analysis at the heterostructure interface—such as transmission electron microscopy (TEM), electron energy loss spectroscopy (EELS), or X-ray photoelectron spectroscopy (XPS)—could help resolve the interdiffusion or strain effects suggested by rocking curve broadening. These techniques would complement the current structural data and clarify how interface quality impacts overall film performance.

Finally, time-of-flight secondary ion mass spectrometry (ToF-SIMS) or depth profiling could reveal compositional gradients within the films or across interfaces, contributing to a more complete picture of growth dynamics and stability.

By building on the structural and electrical foundation laid in this study, these additional approaches will help uncover the fundamental transport properties and interfacial behavior of LSGM and LSCF films, informing future device integration and optimization.

References

1. S.C. Singhal, ‘‘Recent Progress in Tubular Solid Oxide Fuel Cell Technology,’’ in Solid Oxide Fuel Cells V, U. Stimming et al. Ed., The Electrochemical Society, Inc., PV 97–40, pp. 37–50 (1997)
2. A. Matsunaga, Y. Kitanaka, R. Inoue, Y. Noguchi, M. Miyayama, and K. Itaka, “Crystal structures and surface morphologies of LaGaO 3 -based epitaxial thin films grown by a pulse laser deposition method,” Key Engineering Materials **582**, (2013).
3. T. Ishihara, H. Matsuda, Y. Takita, J. Am. Chem. Soc. 116, 3801 (1994)
4. T. Ishihara, ‘‘Chapter 79. Novel electrolytes operating at 400–600 C,’’ Fuel Cell Handbook Vol. 4, pp. 1109–1122 (2003)
5. S. Li, “Preparation and characterization of perovskite structure lanthanum gallate and lanthanum aluminate based oxides,” DIVA, (2022).
6. K. Huang, J.B. Goodenough, J. Alloys Compd. 303–304, 454 (2000)
7. P. Datta, P. Majewski, F. Aldinger, J. Alloys Compd. 438, 232 (2007)
8. A. Matraszek, L. Singheiser, D. Kobertza, K. Hilpert, M. Miller, O. Schulz, M. Martin, Solid State Ionics 166, 343 (2004)
9. S.B. Adler, “Factors Governing Oxygen Reduction in Solid Oxide Fuel Cell Cathodes,” Chemical Reviews **104**(10), 4791–4844 (2004).
10. S.P. Jiang, “Development of lanthanum strontium cobalt ferrite perovskite electrodes of solid oxide fuel cells – A review,” International Journal of Hydrogen Energy **44**(14), 7448–7493 (2019).
11. N. Sakai, H. Kishimoto, K. Yamaji, T. Horita, M.E. Brito, H. Yokokawa, J. Electro-chem. Soc., 154, B1331 (2007)

12. L. Blum, P. Batfalsky, L.G.J. de Haart, J. Malzbender, N.H. Menzler, R. Peters, W.J. Quadakkers, J. Remmel, F. Tietz, and D. Stolten, “Overview on the Jülich SOFC Development Status,” ECS Transactions **57**(1), 23–33 (2013).
13. H. Yokokawa, ‘‘Recent Developments in Solid Oxide Fuel Cell Materials,’’ Fuel Cells Fundam. Syst. 1(2), 1–15 (2001)
14. H. Yokokawa, N. Sakai, T. Horita, K. Yamaji, M.E. Brito, ‘‘Solid Oxide Electrolytes for High Temperature Fuel Cells,’’ Electrochemistry 73, 20–30 (2005)
15. J. Jiang et al., Appl. Phys. Lett.**102**, 173504 (2013)
16. E. Gilardi et al., Phys. Chem. Chem. Phys.**20**, 19995 (2018)
17. N.A. Shepelin, Z.P. Tehrani, N. Ohannessian, C.W. Schneider, D. Pergolesi, and T. Lippert, “A practical guide to pulsed laser deposition,” Chemical Society Reviews **52**(7), 2294–2321 (2023).
18. A. Zomorrodian, Hadi Salamati, Z. Lu, X. Chen, N. Wu, and A. Ignatiev, “Electrical conductivity of epitaxial La0.6Sr0.4Co0.2Fe0.8O3−δ thin films grown by pulsed laser deposition,” International Journal of Hydrogen Energy **35**(22), 12443–12448 (2010).
19. N. Yang, A. D'Epifanio, E. Di Bartolomeo, C. Pugnalini, A. Tebano, G. Balestrino, and S. Licoccia, “La0.8Sr0.2Ga0.8Mg0.2O3 − δ thin films for IT-SOFCs: Microstructure and transport properties correlation,” Journal of Power Sources **222**, 10–14 (2012).
20. J. Hwang, H. Lee, J.-H. Lee, K.J. Yoon, H. Kim, J. Hong, and J.-W. Son, “Specific considerations for obtaining appropriate La1−xSrxGa1−yMgyO3−δ thin films using pulsed-laser deposition and its influence on the performance of solid-oxide fuel cells,” Journal of Power Sources **274**, 41–47 (2014).

21. P. Plonczak, A. Bieberle-Hütter, M. Søgaard, T. Ryll, J. Martynczuk, P.V. Hendriksen, and L.J. Gauckler, "Tailoring of $La_xSr_{1-x}Co_yFe_{1-y}O_{3-\delta}$ Nanostructure by Pulsed Laser Deposition," Advanced Functional Materials **21**(14), 2764–2775 (2011).
22. M. Xu, J. Yu, Y. Song, R. Ran, W. Wang, and Z. Shao, "Advances in Ceramic Thin Films Fabricated by Pulsed Laser Deposition for Intermediate-Temperature Solid Oxide Fuel Cells," Energy & Fuels **34**(9), 10568–10582 (2020).
23. G.F. Harrington, and J. Santiso, "Back-to-Basics tutorial: X-ray diffraction of thin films," Journal of Electroceramics **47**, (2021).
24. C. Suryanarayana, and N.M. Grant, *X-Ray Diffraction a Practical Approach.* (Springer Verlag, 2014), pp. 153–157.
25. Bernard Denis Cullity, S.R. Stock, and I. Education, *Elements of X-Ray Diffraction* (Pearson India Education Services, Miejsce Nieznane, 2015), pp. 171–175.
26. F. Tietz, V.A.C. Haanappel, A. Mai, J. Mertens, and D. Stöver, "Performance of LSCF cathodes in cell tests," Journal of Power Sources **156**(1), 20–22 (2006).

Supplemental

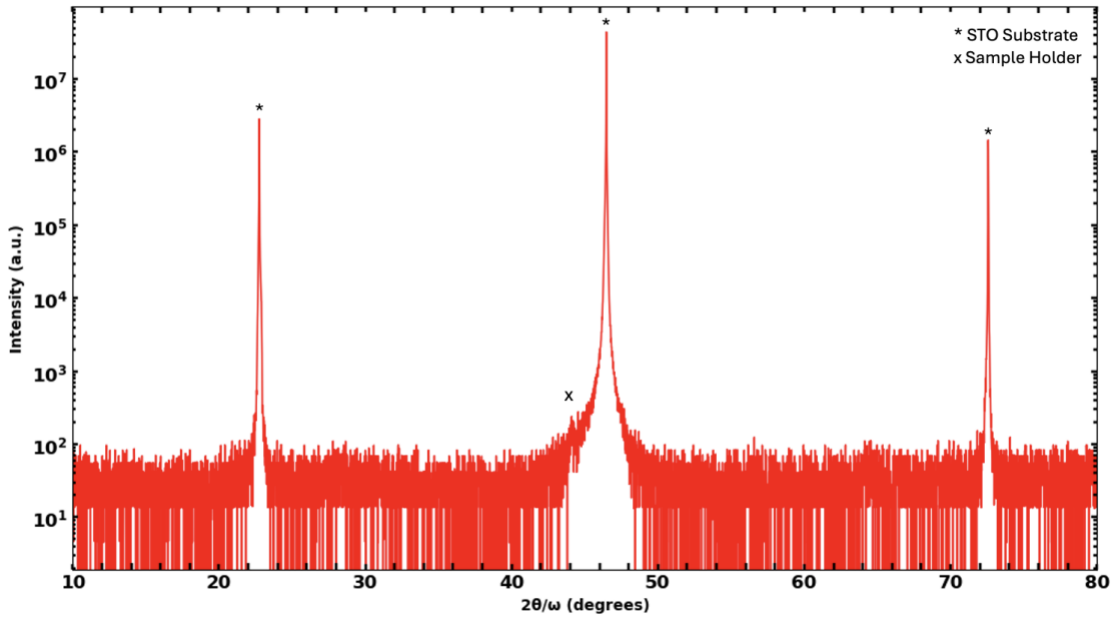

Figure 38:XRD scan of LSGM film grown at 600°C and 100mTorr

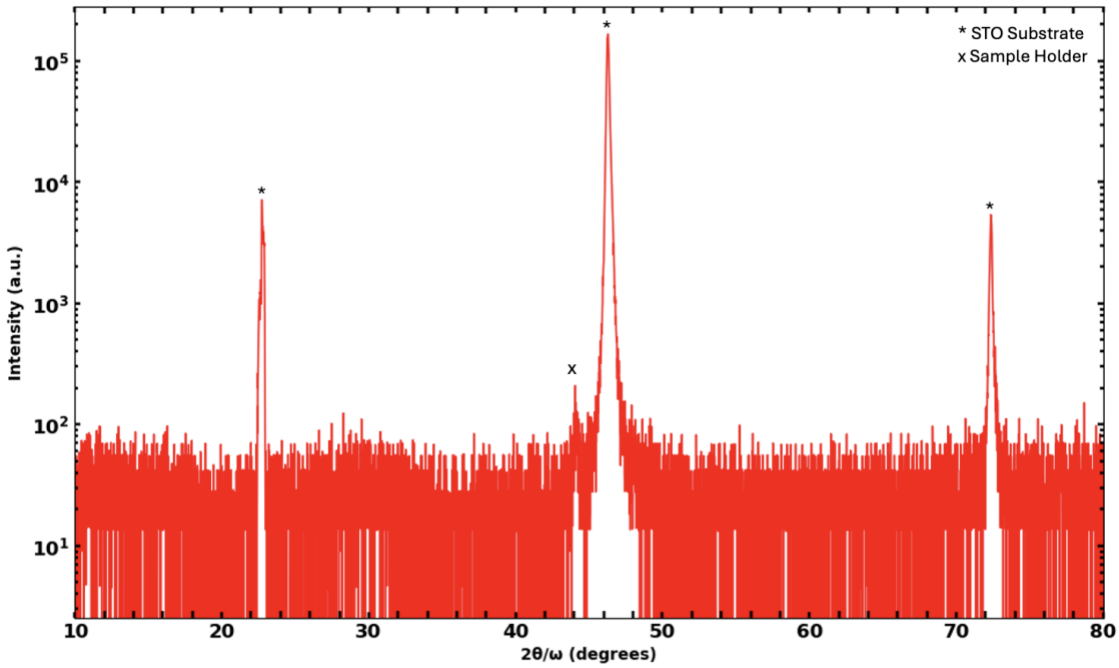

Figure 39:XRD scan of LSGM film grown at 700°C and 100mTorr

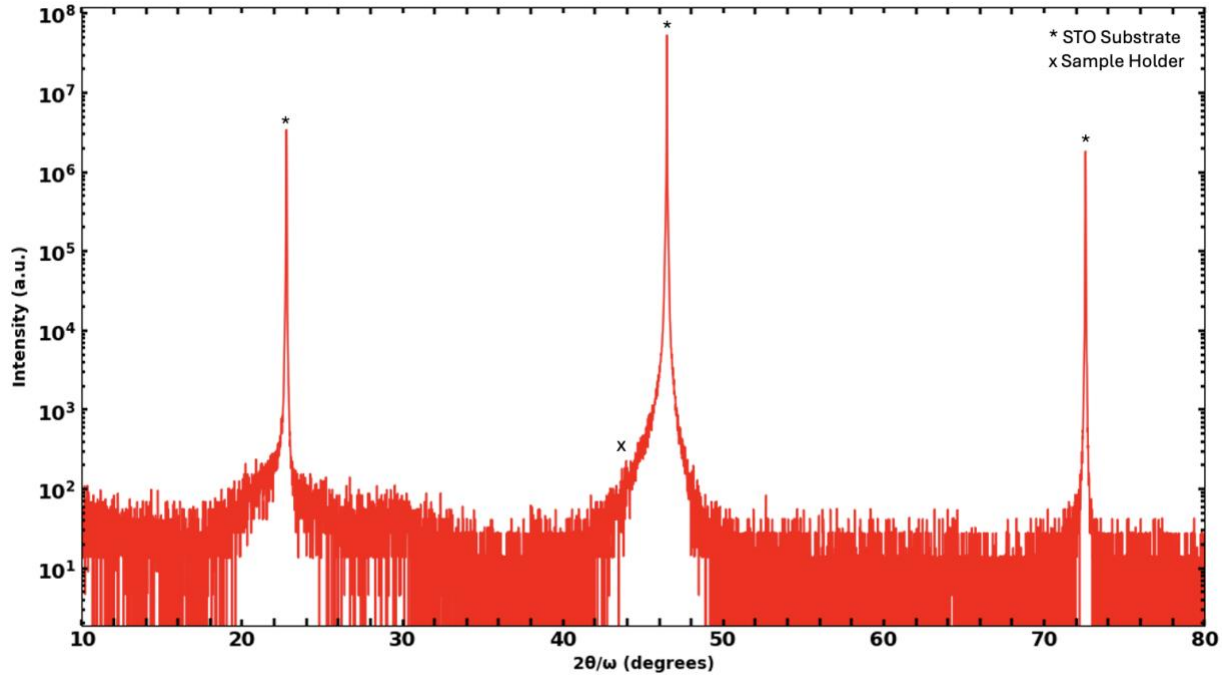

Figure 40:XRD scan of LSGM film grown at 800°C and 100mTorr

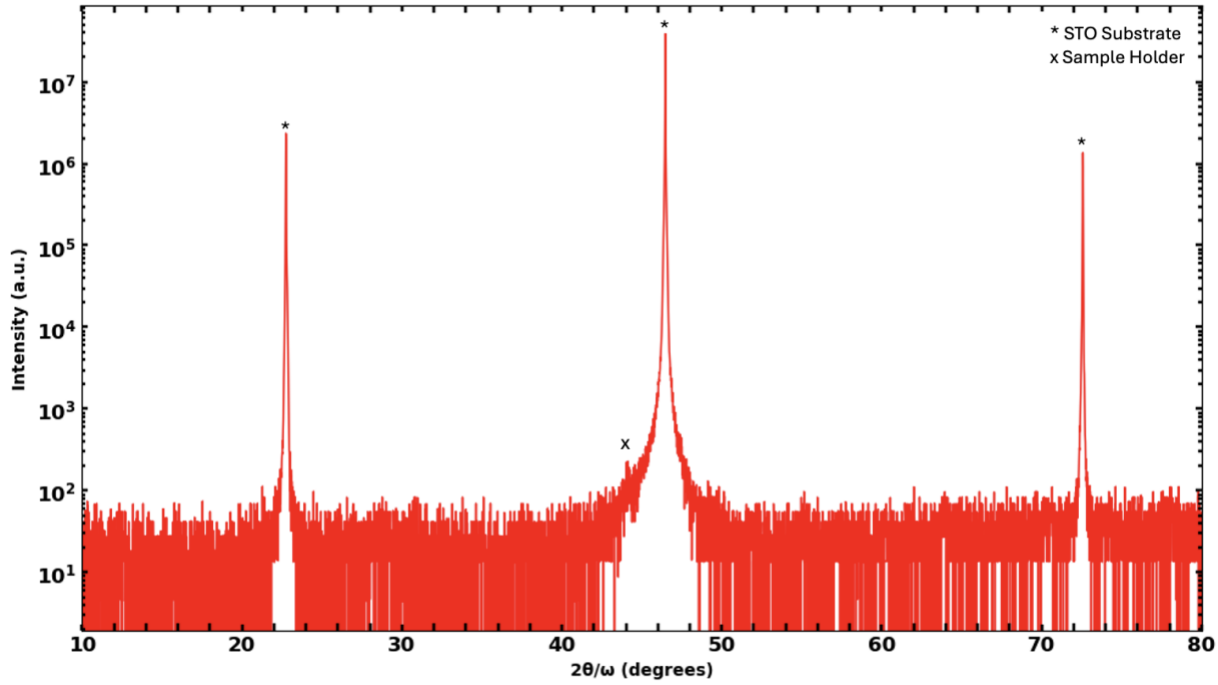

Figure 41:XRD scan of LSGM film grown at 600°C and 150mTorr

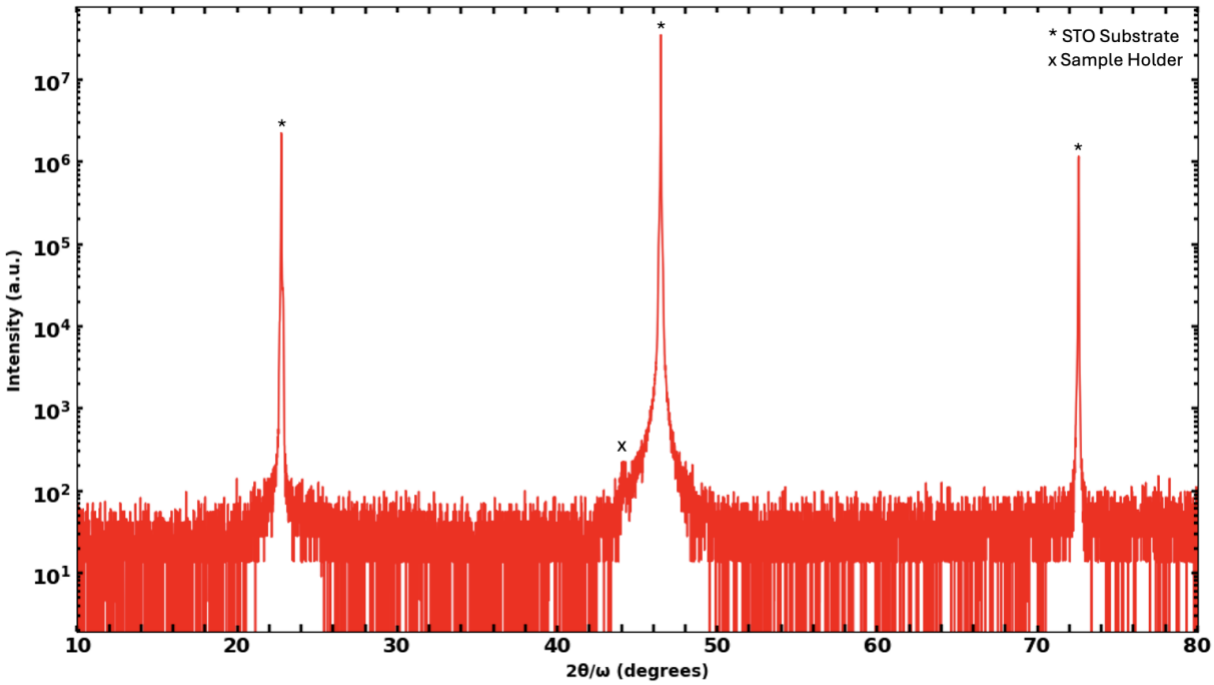

Figure 42:XRD scan of LSGM film grown at 700°C and 150mTorr

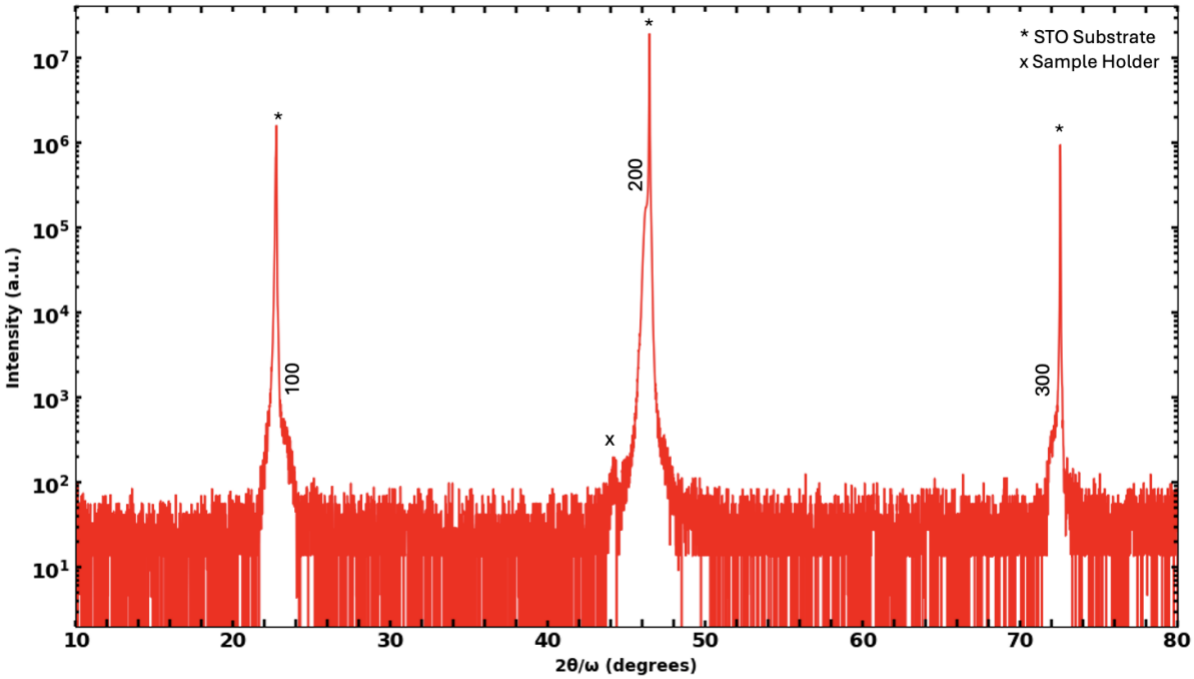

Figure 43:XRD scan of LSGM film grown at 800°C and 150mTorr

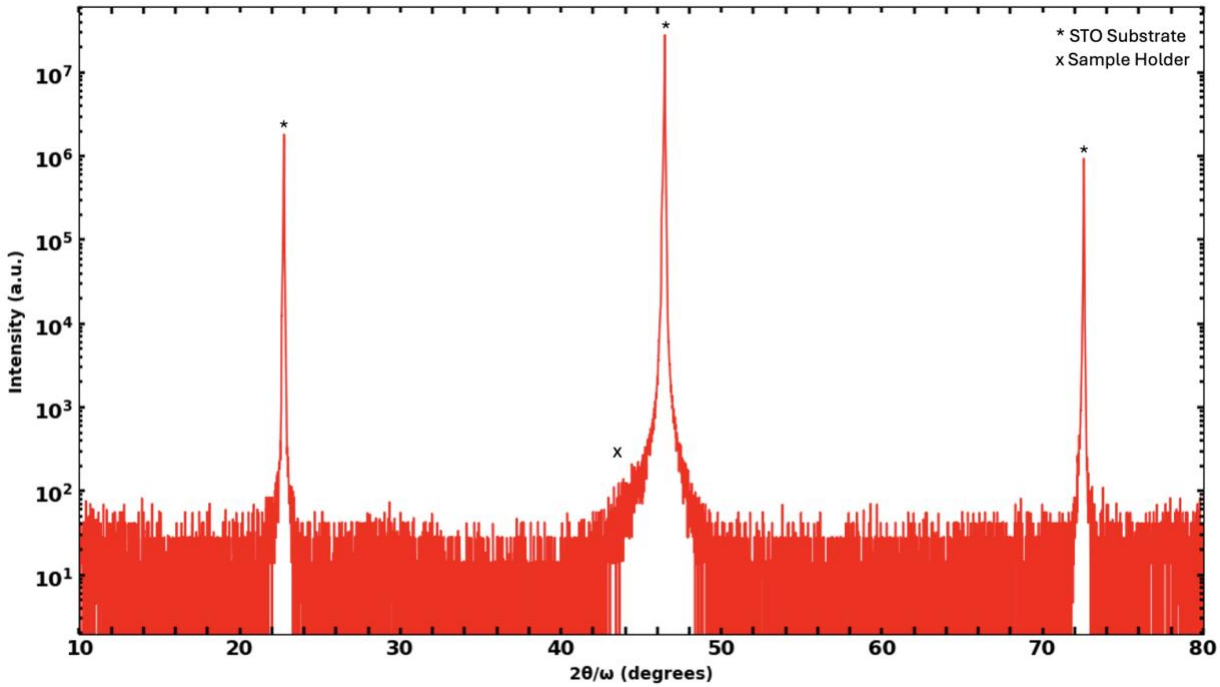

Figure 44:XRD scan of LSGM film grown at 600°C and 200mTorr

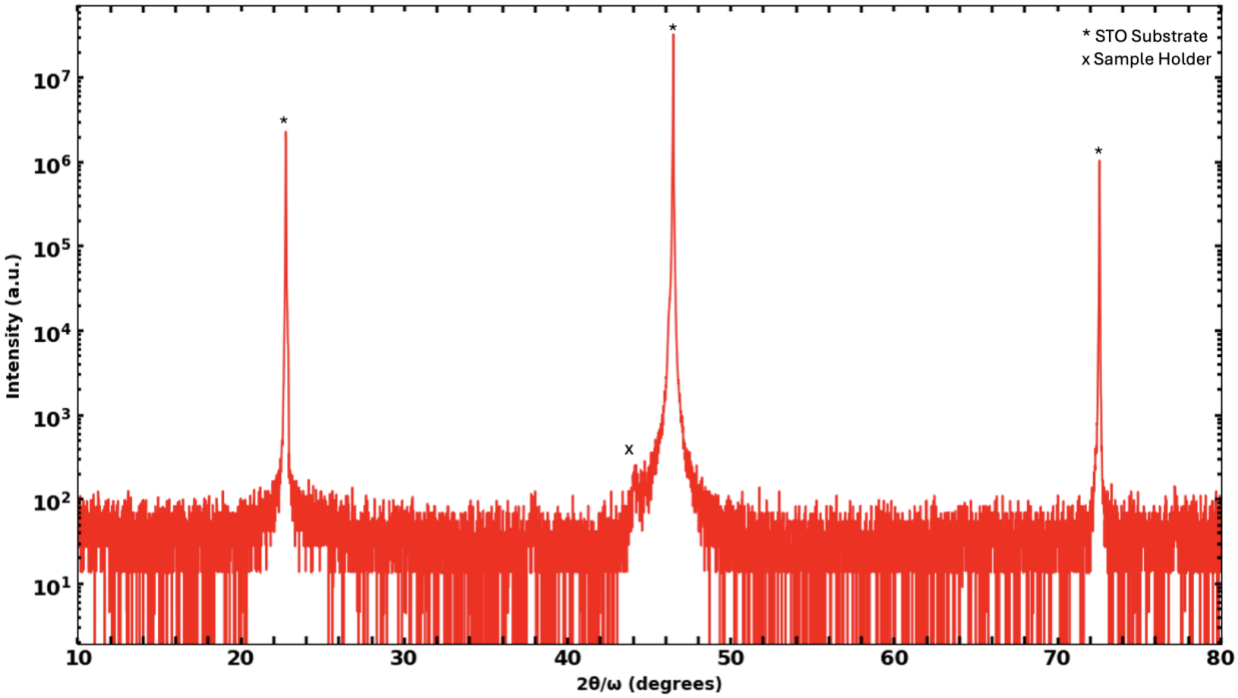

Figure 45:XRD scan of LSGM film grown at 700°C and 200mTorr

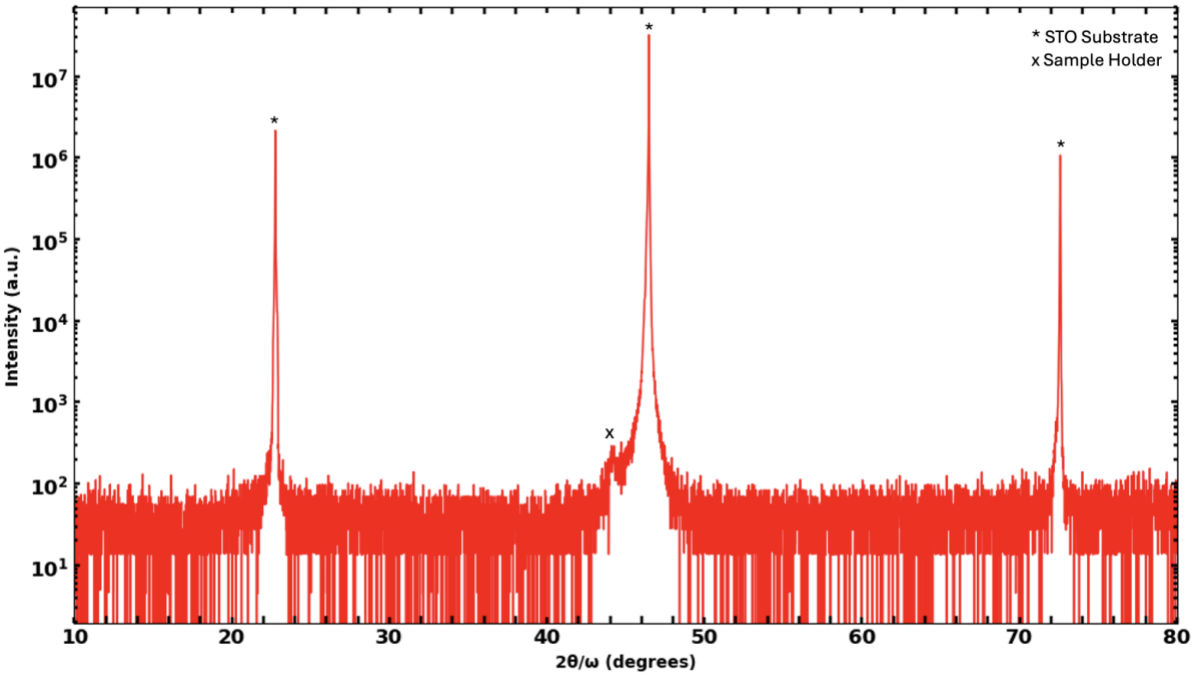

Figure 46:XRD scan of LSGM film grown at 800°C and 200mTorr

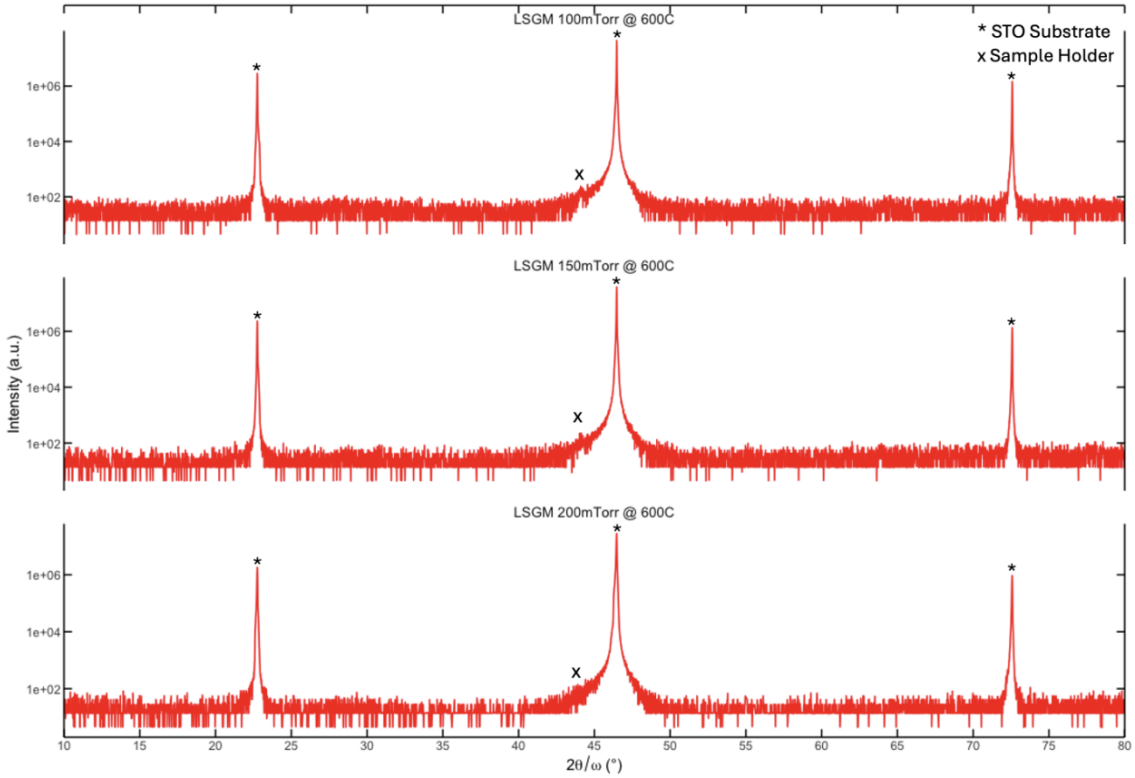

Figure 47: XRD of LSGM films grown at 600°C pressure comparison

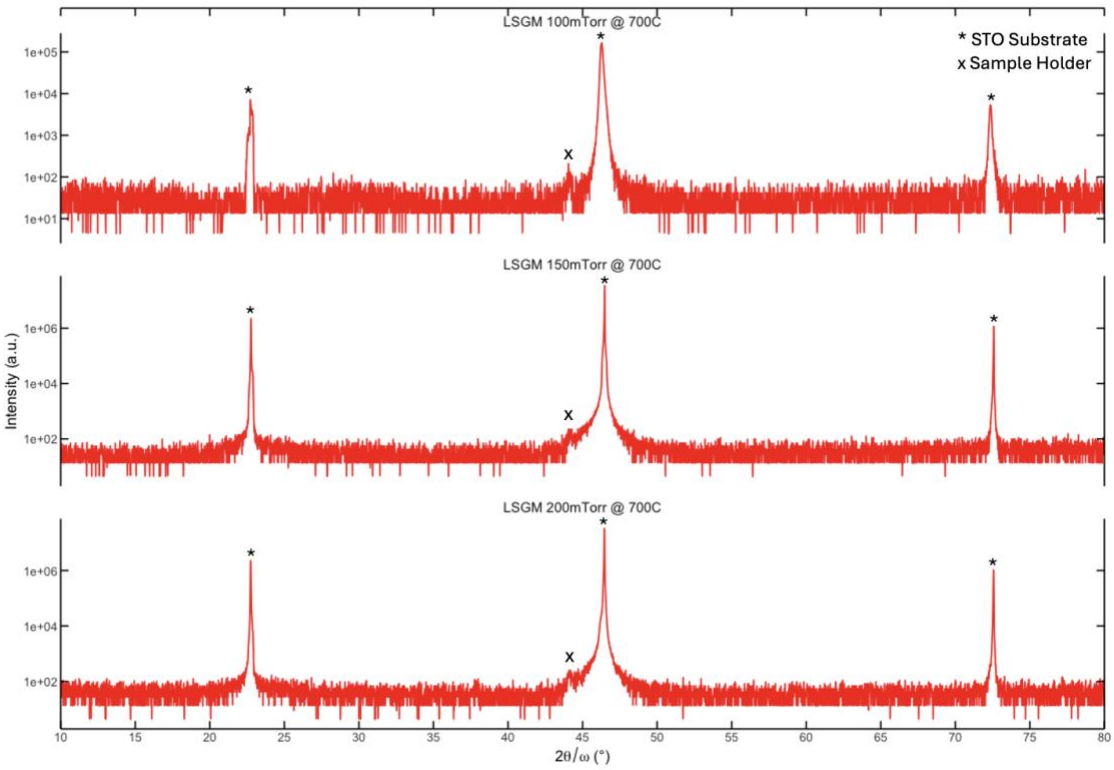

Figure 48:XRD of LSGM films grown at 700°C pressure comparison

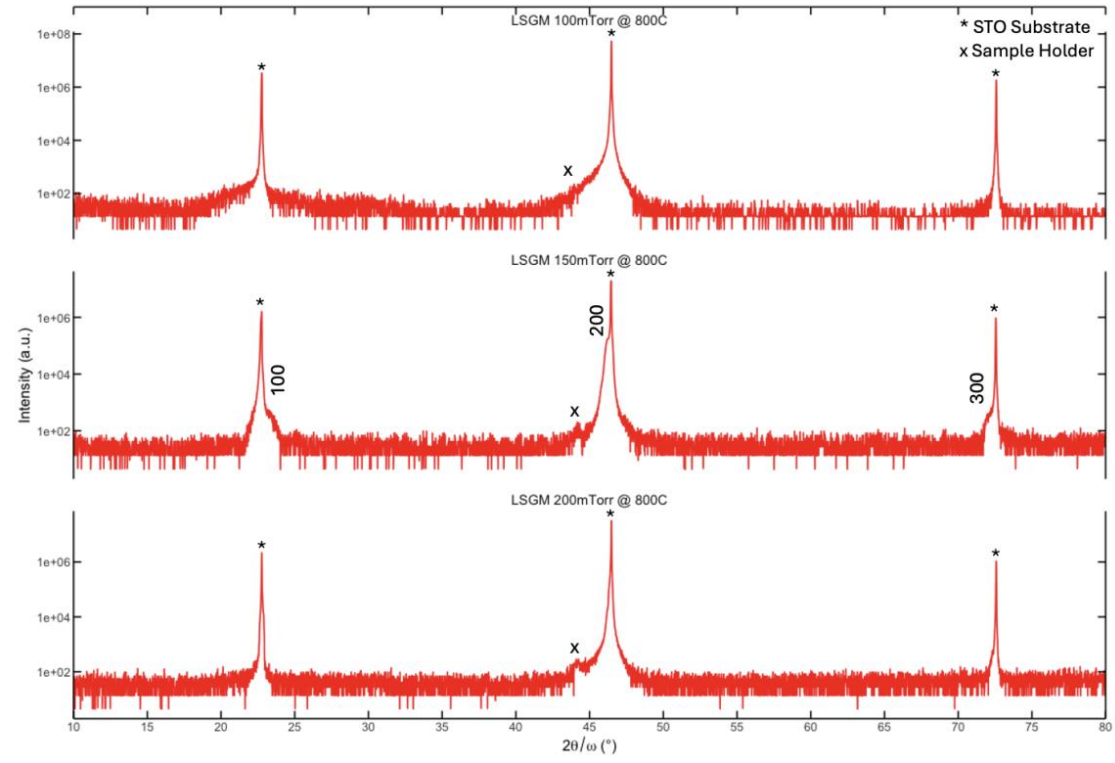

Figure 49:XRD of LSGM films grown at 800°C pressure comparison

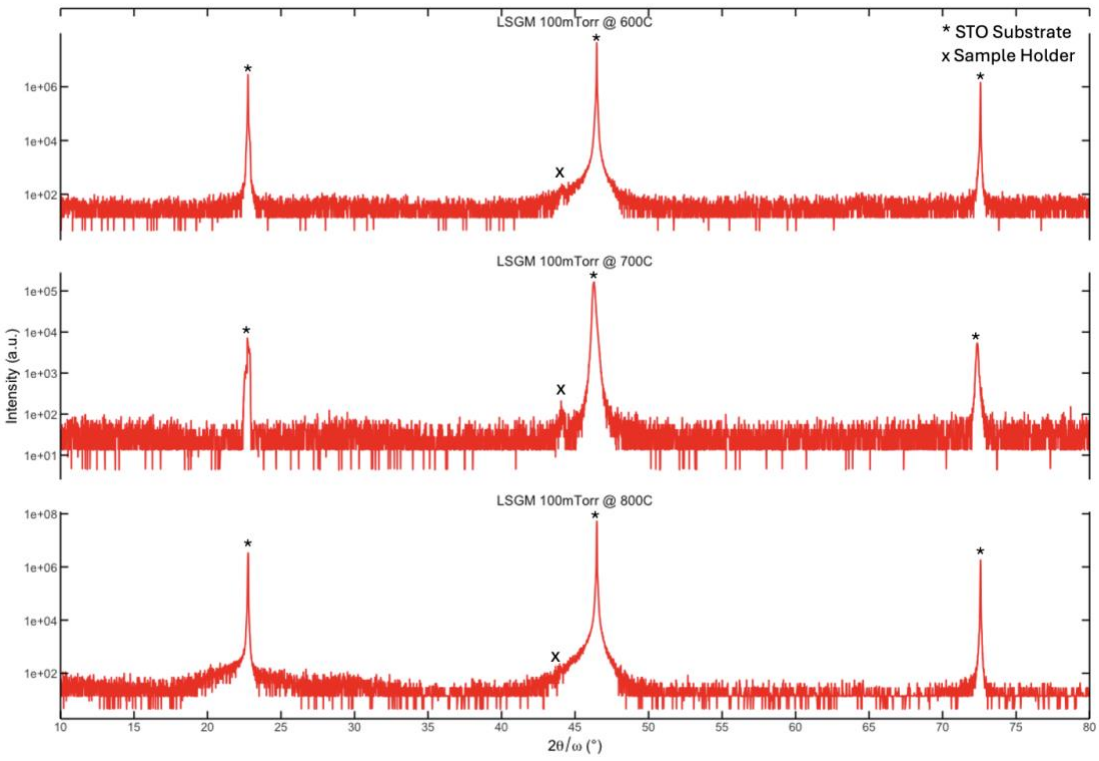

Figure 50:XRD of LSGM films grown at 100mTorr temperature comparison

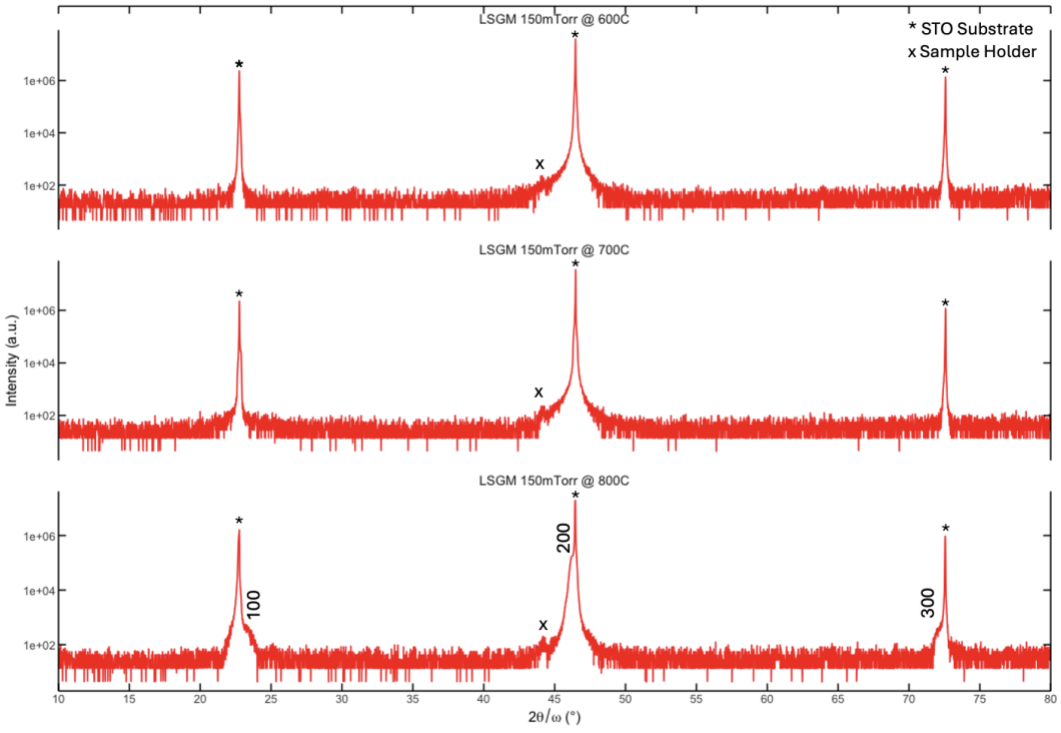

Figure 51:XRD of LSGM films grown at 150mTorr temperature comparison

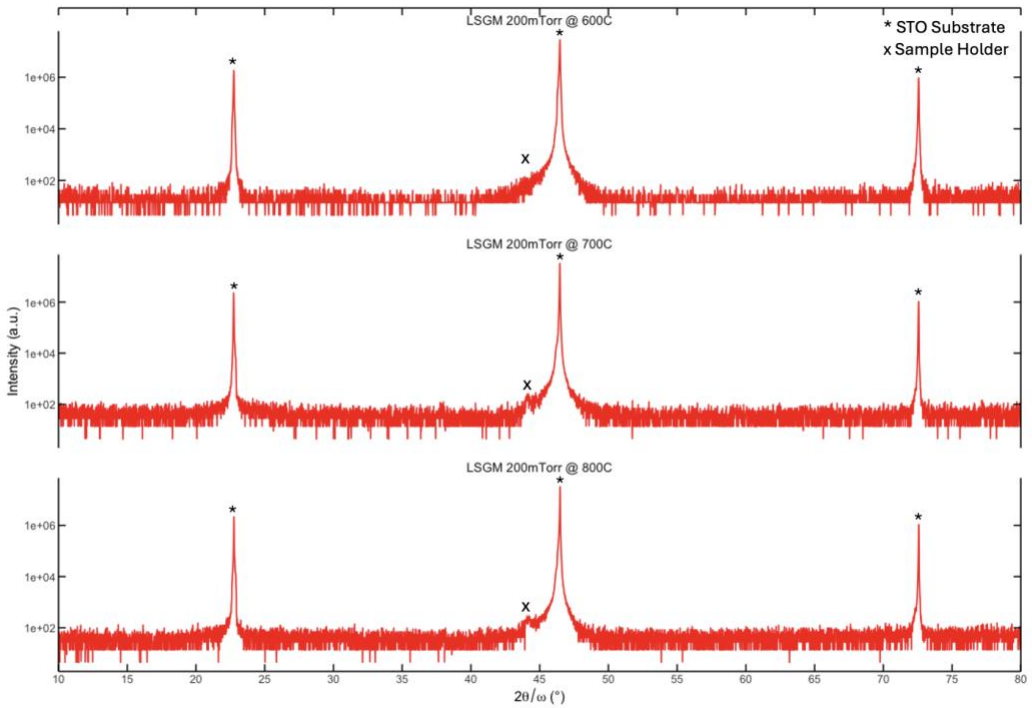

Figure 52:XRD of LSGM films grown at 200mTorr temperature comparison

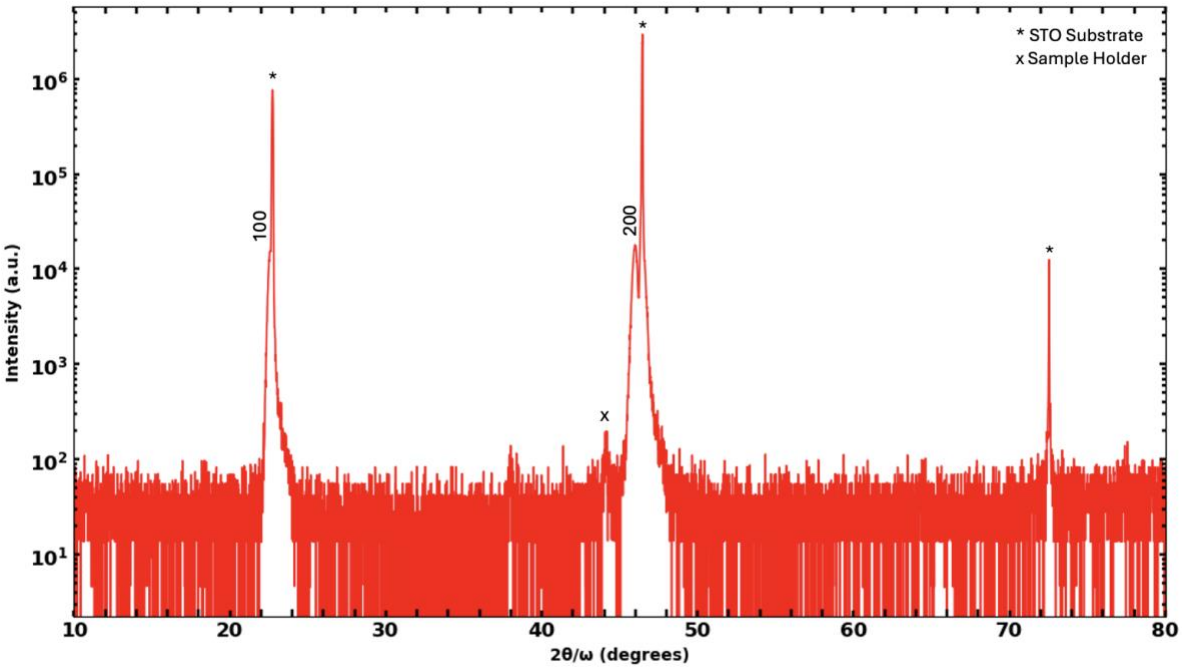

Figure 53:XRD scan of LSCF film grown at 600°C and 100mTorr

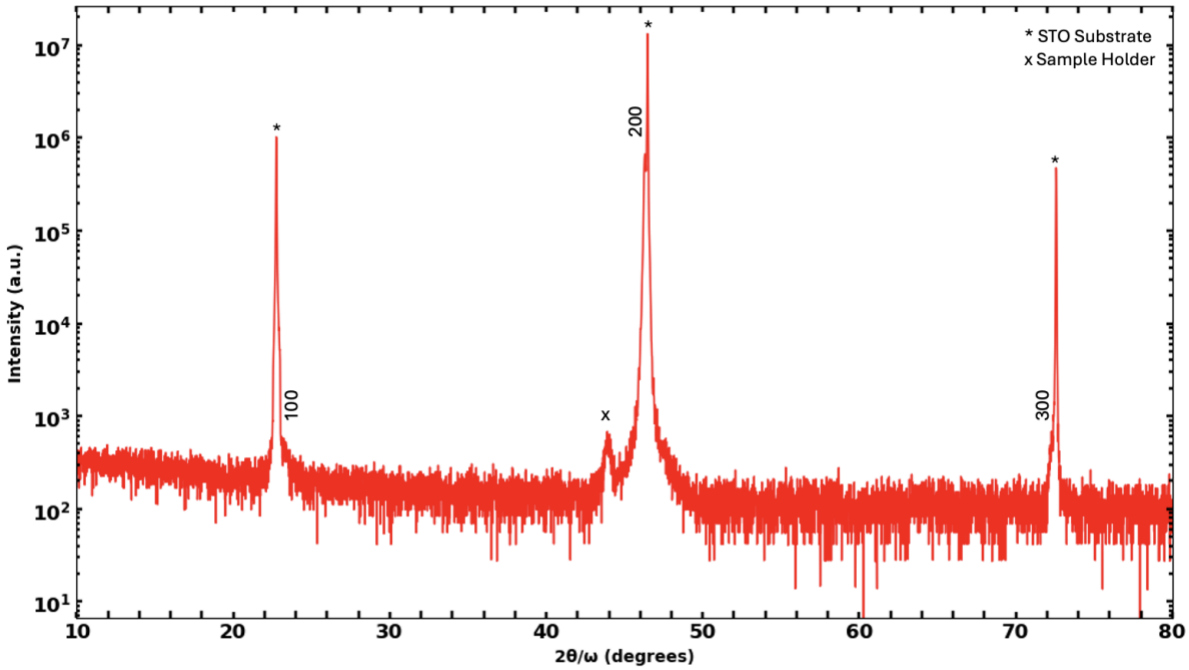

Figure 54:XRD scan of LSCF film grown at 700°C and 100mTorr

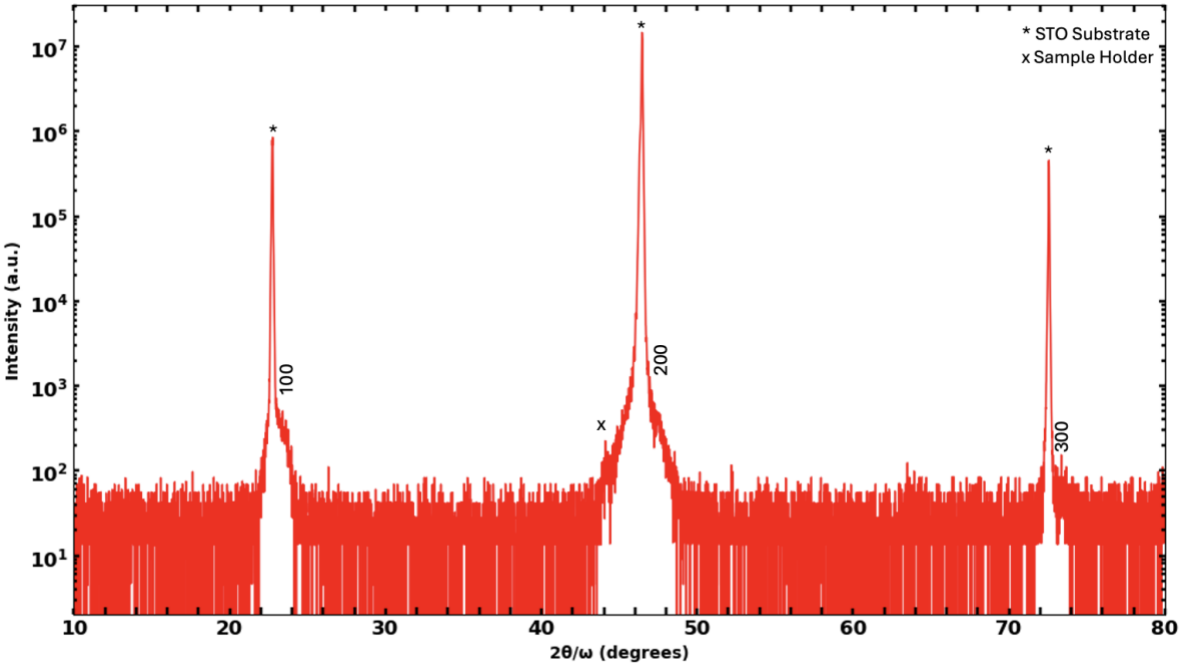

Figure 55:XRD scan of LSCF film grown at 800°C and 100mTorr

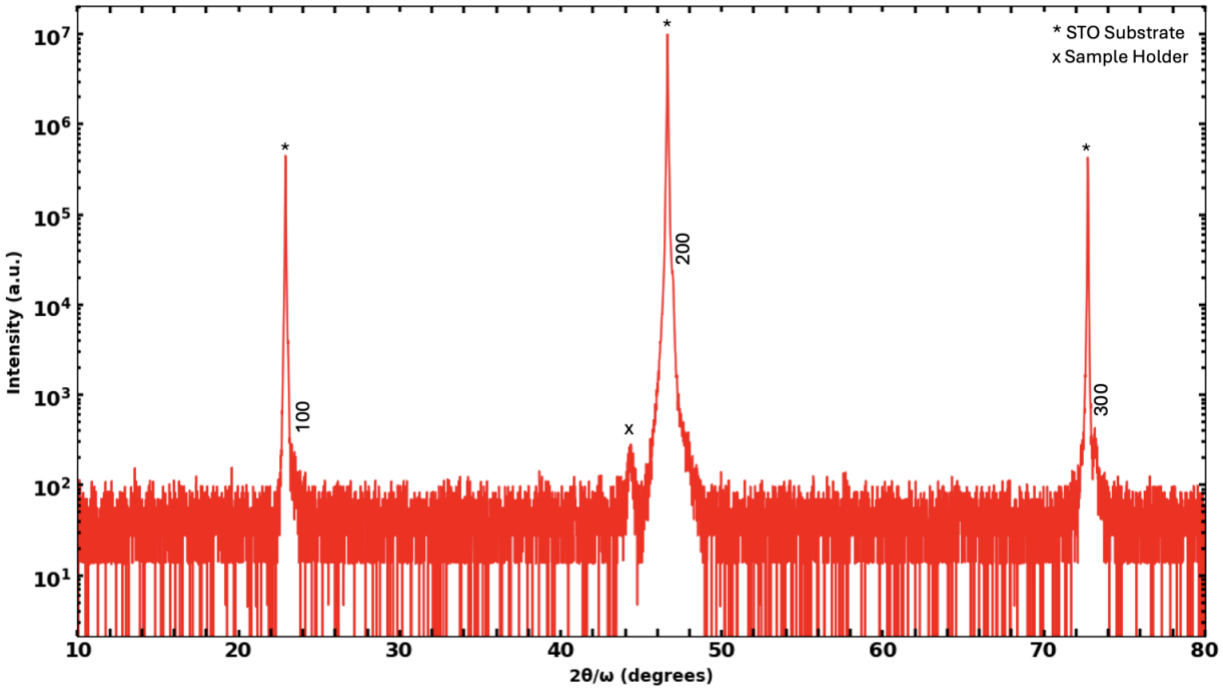

Figure 56:XRD scan of LSCF film grown at 600°C and 150mTorr

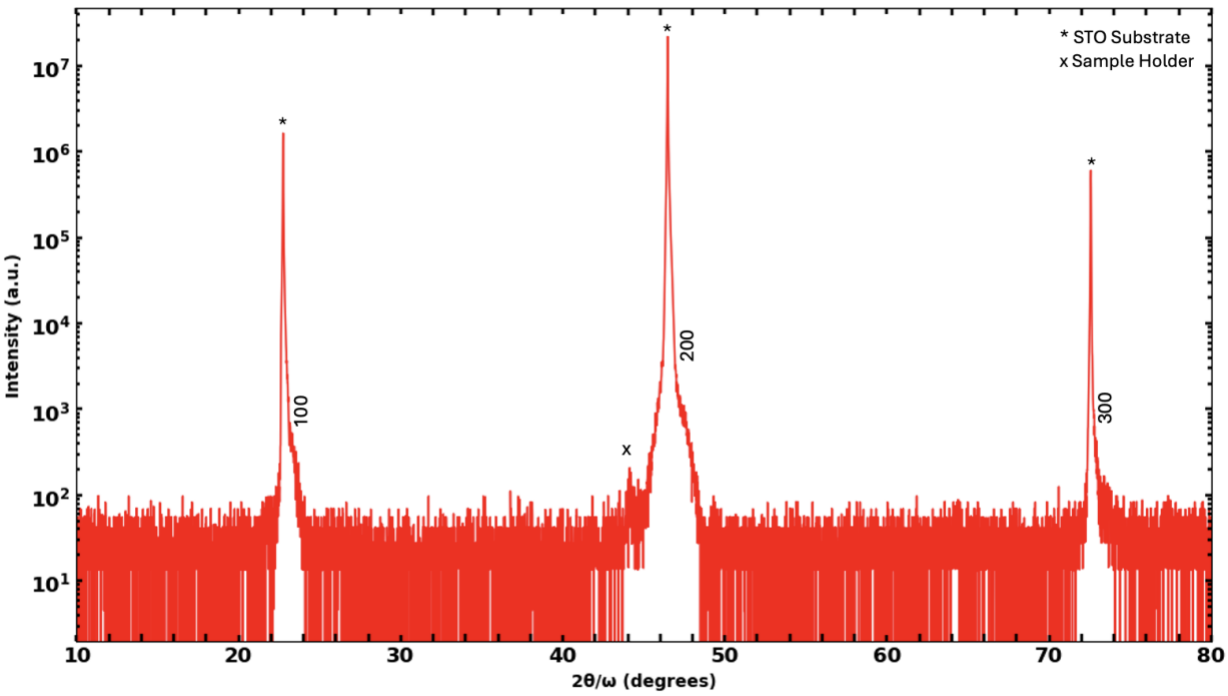

Figure 57:XRD scan of LSCF film grown at 700°C and 150mTorr

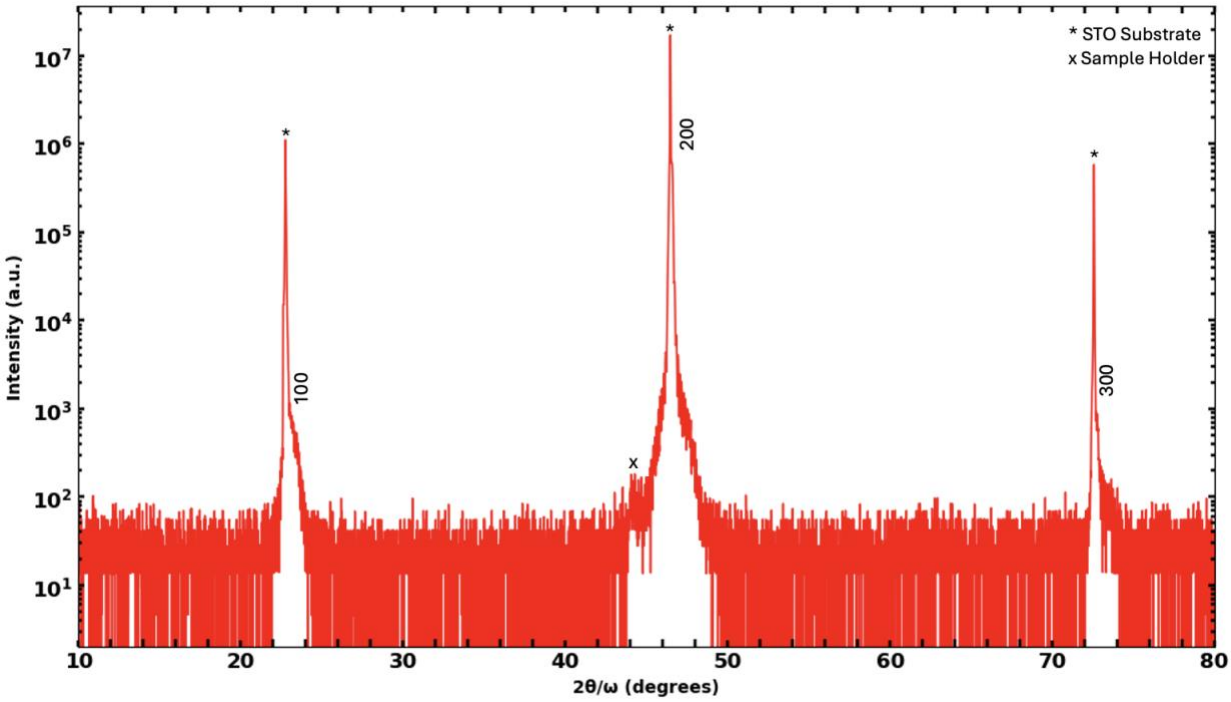

Figure 58:XRD scan of LSCF film grown at 800°C and 150mTorr

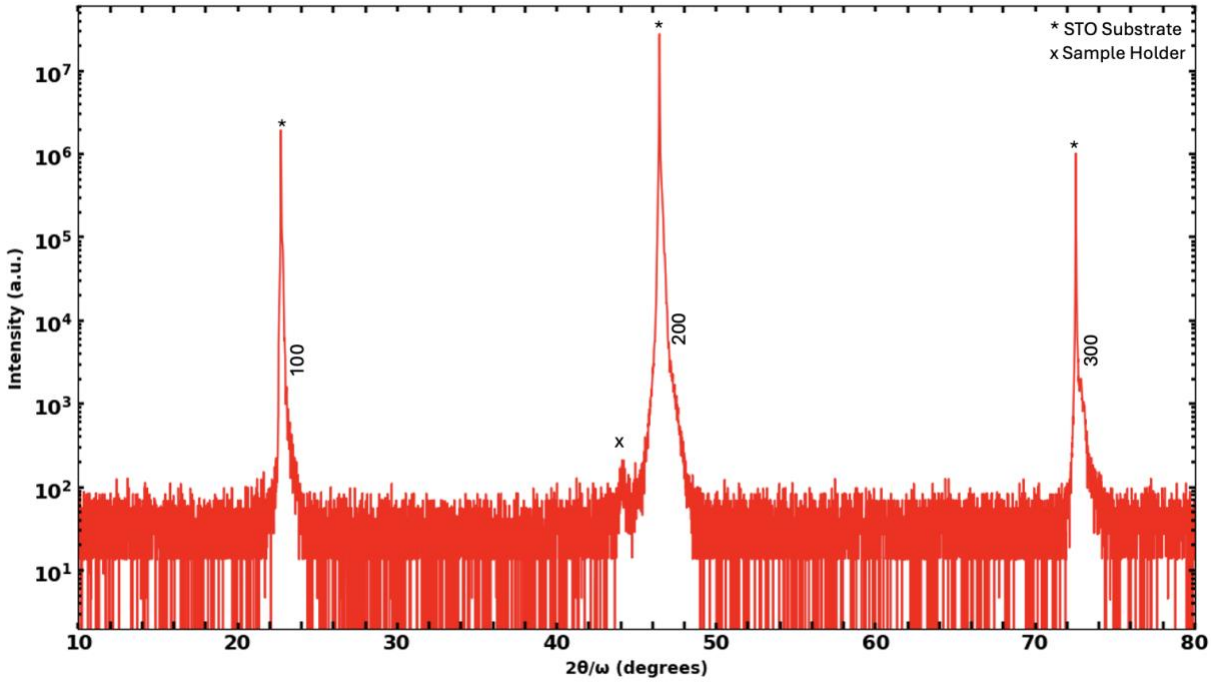

Figure 59:XRD scan of LSCF film grown at 600°C and 200mTorr

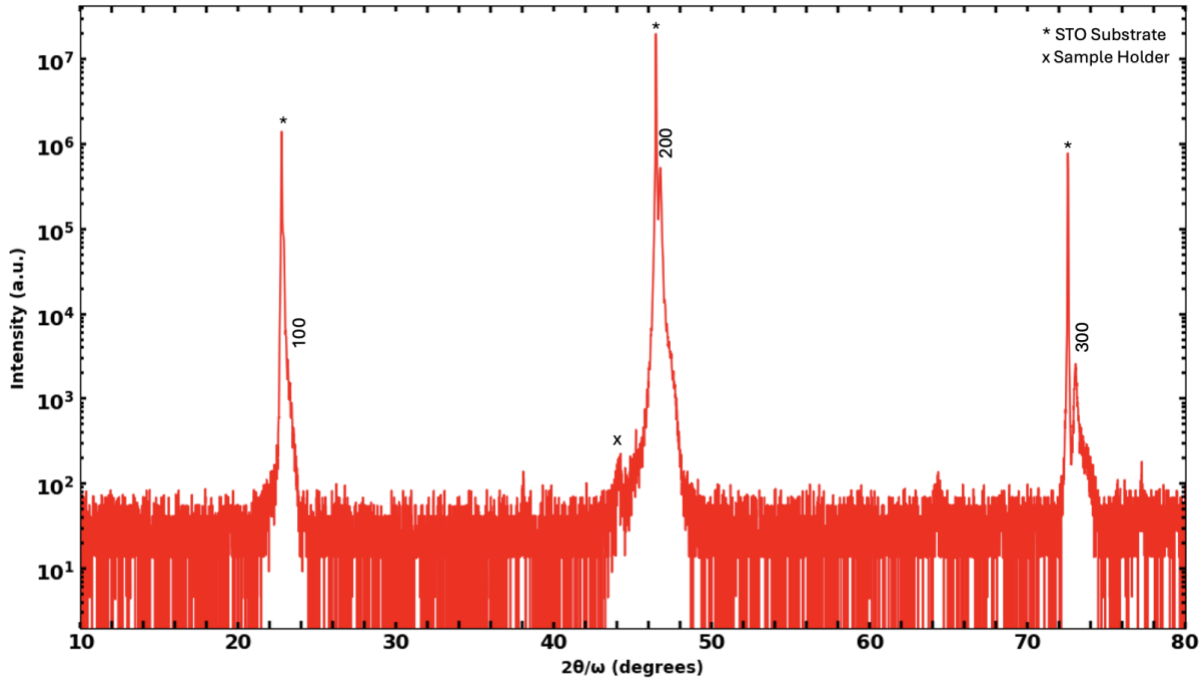

Figure 60:XRD scan of LSCF film grown at 700°C and 200mTorr

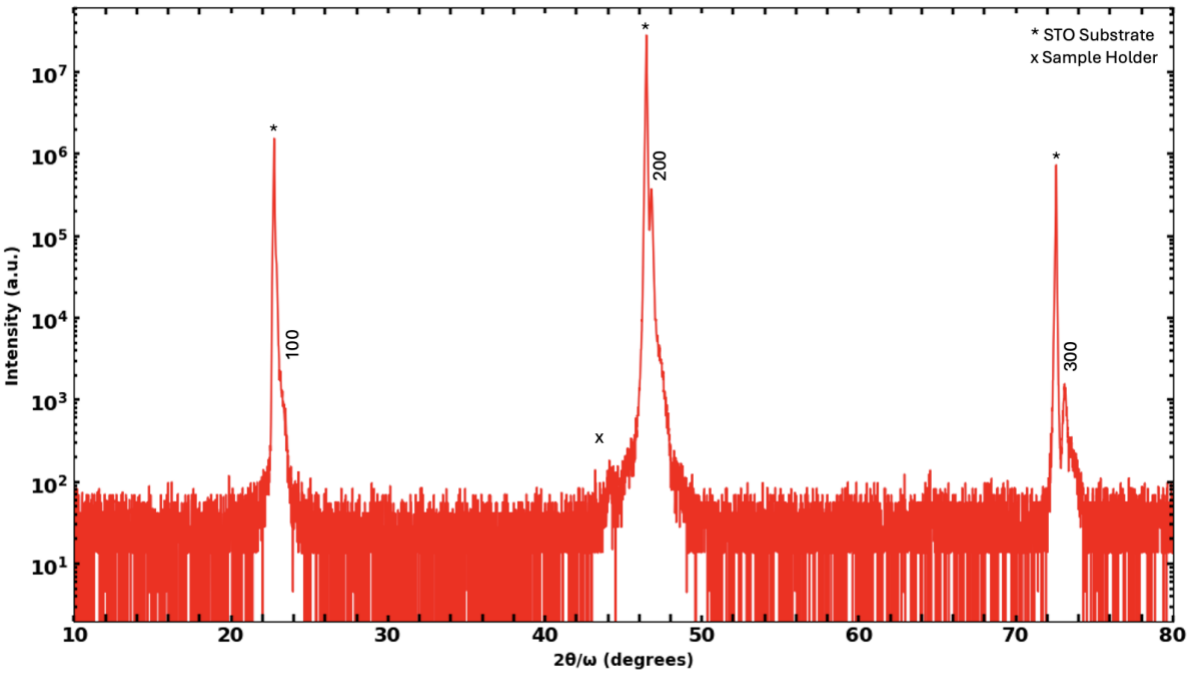

Figure 61:XRD scan of LSCF film grown at 800°C and 200mTorr

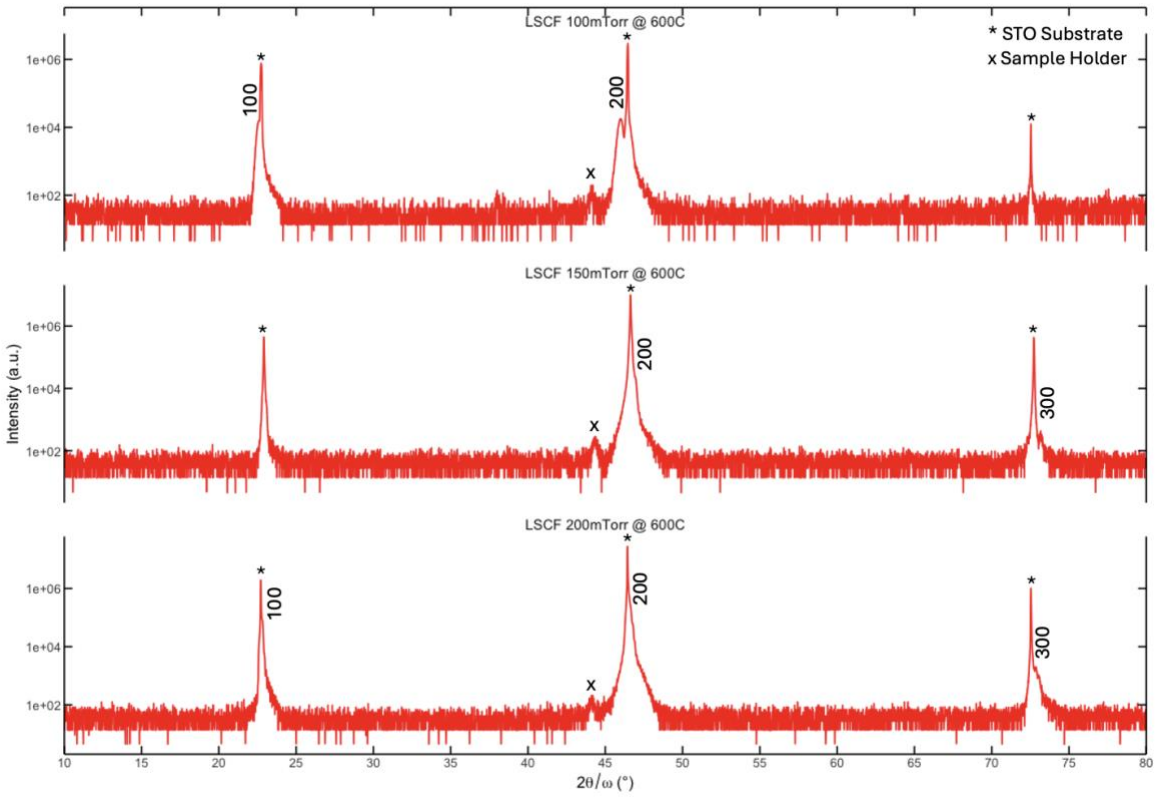

Figure 62:XRD of LSCF films grown at 600°C pressure comparison

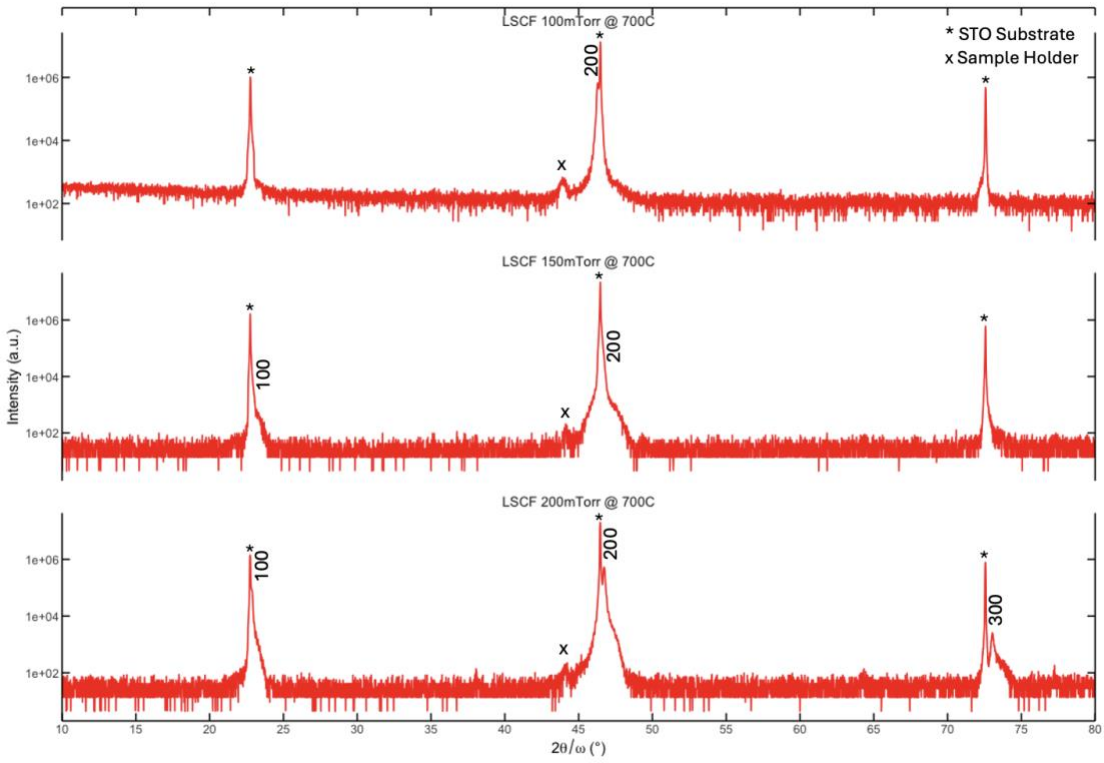

Figure 63:XRD of LSCF films grown at 700°C pressure comparison

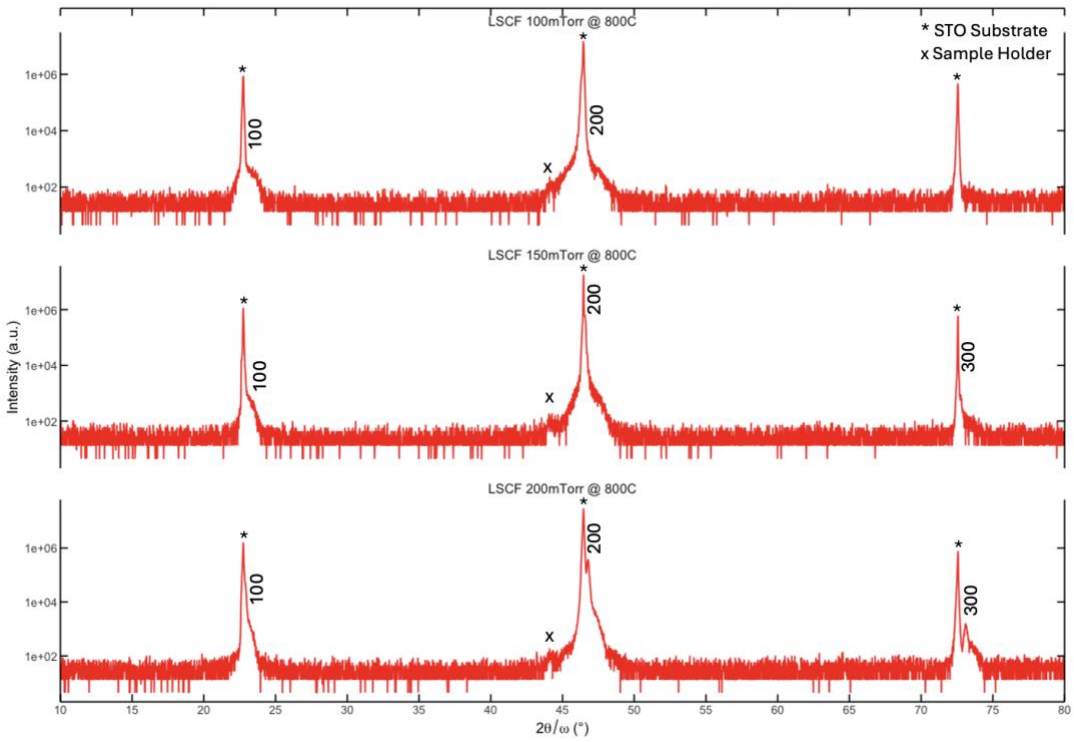

Figure 64:XRD of LSCF films grown at 800°C pressure comparison

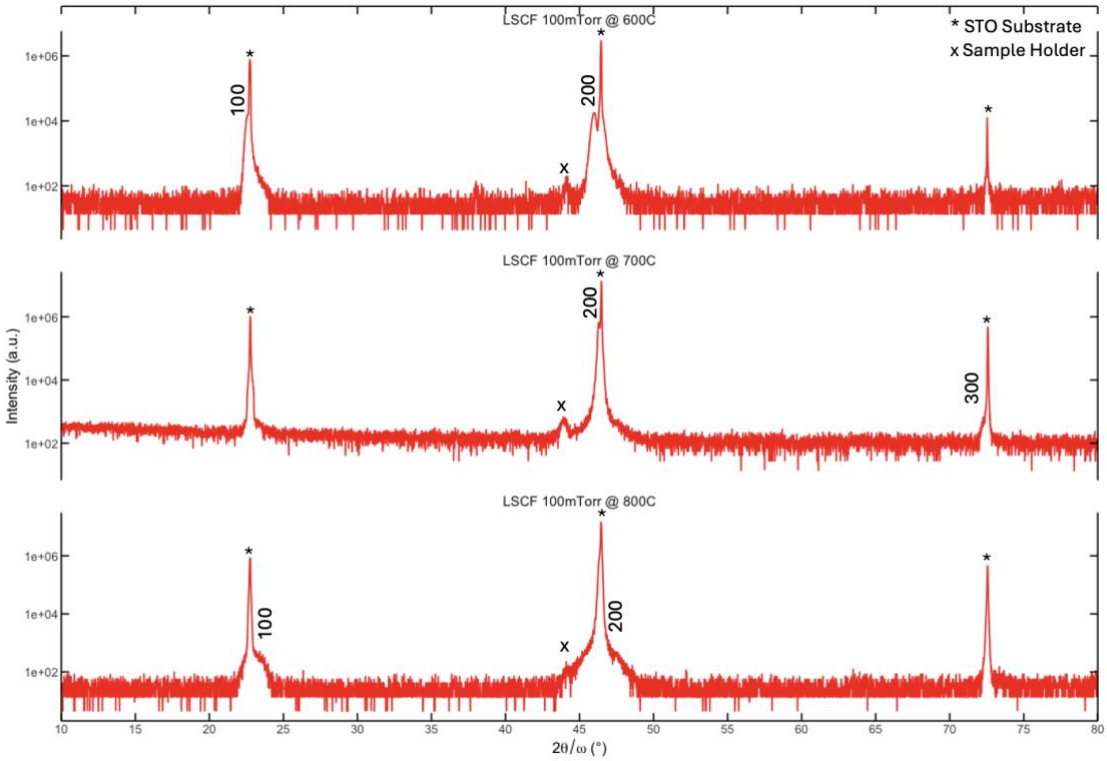

Figure 65:XRD of LSCF films grown at 100mTorr temperature comparison

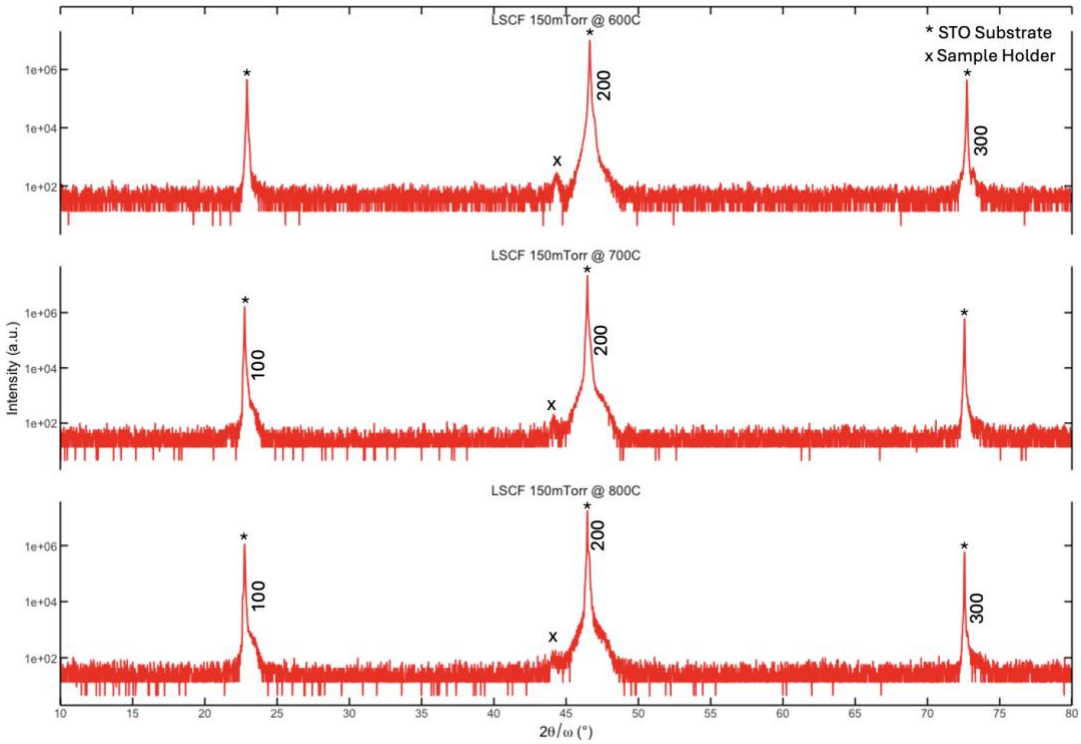

Figure 66:XRD of LSCF films grown at 150mTorr temperature comparison

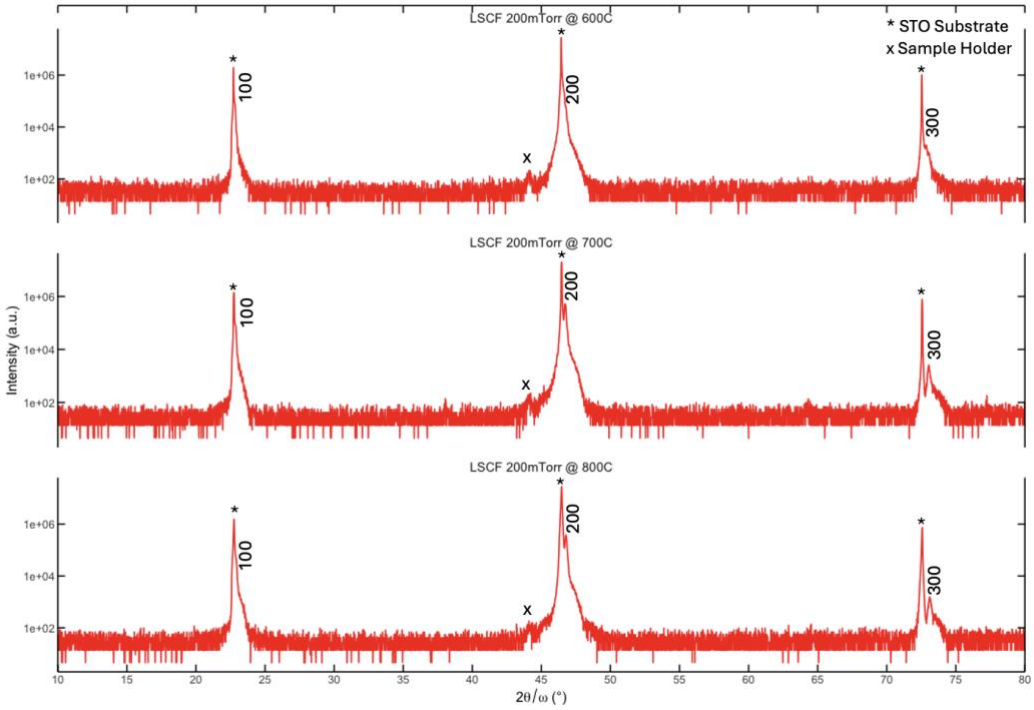

Figure 67:XRD of LSCF films grown at 200mTorr temperature comparison

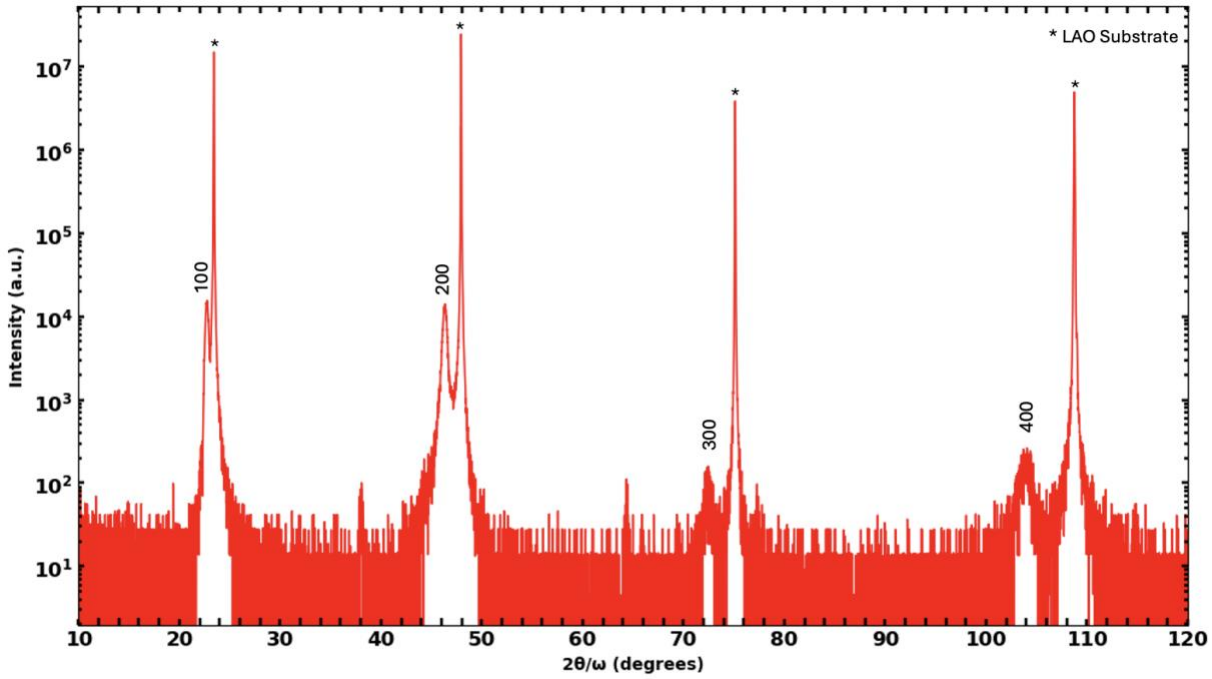

Figure 68:XRD scan of LSGM film grown at 800°C and 150mTorr on LAO

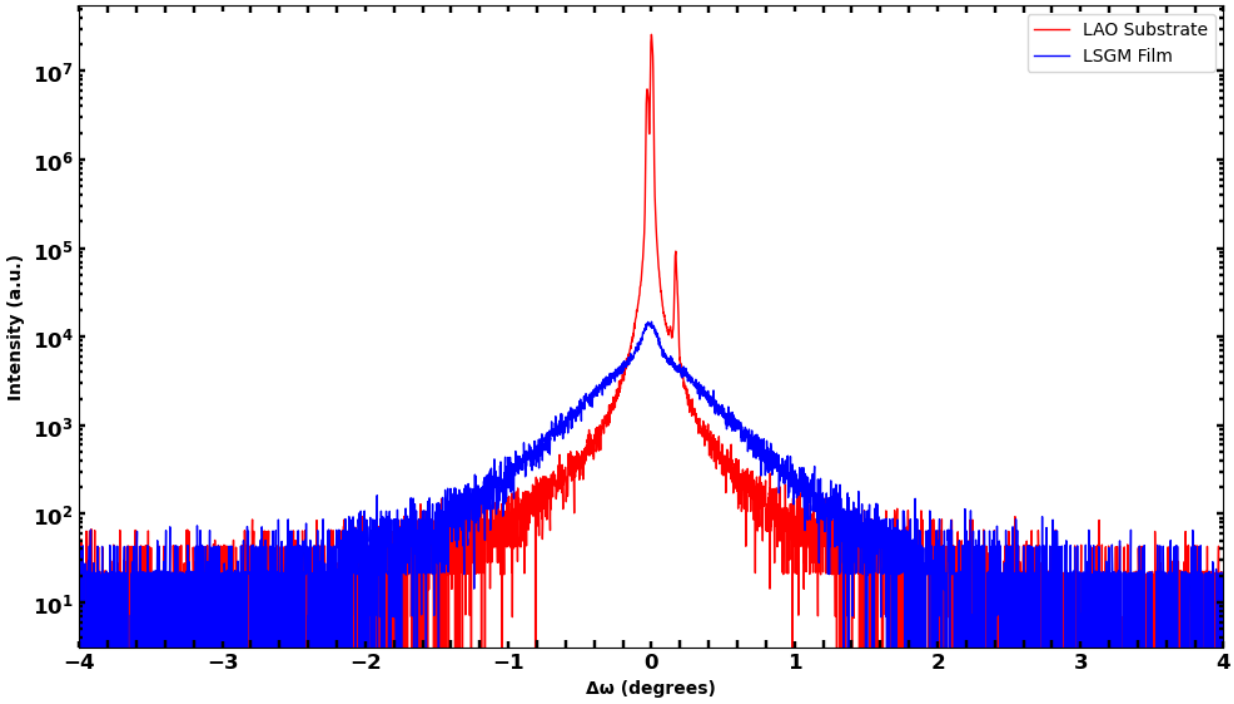

Figure 69:RC 200 scan of LSGM film grown at 800°C and 150mTorr on LAO

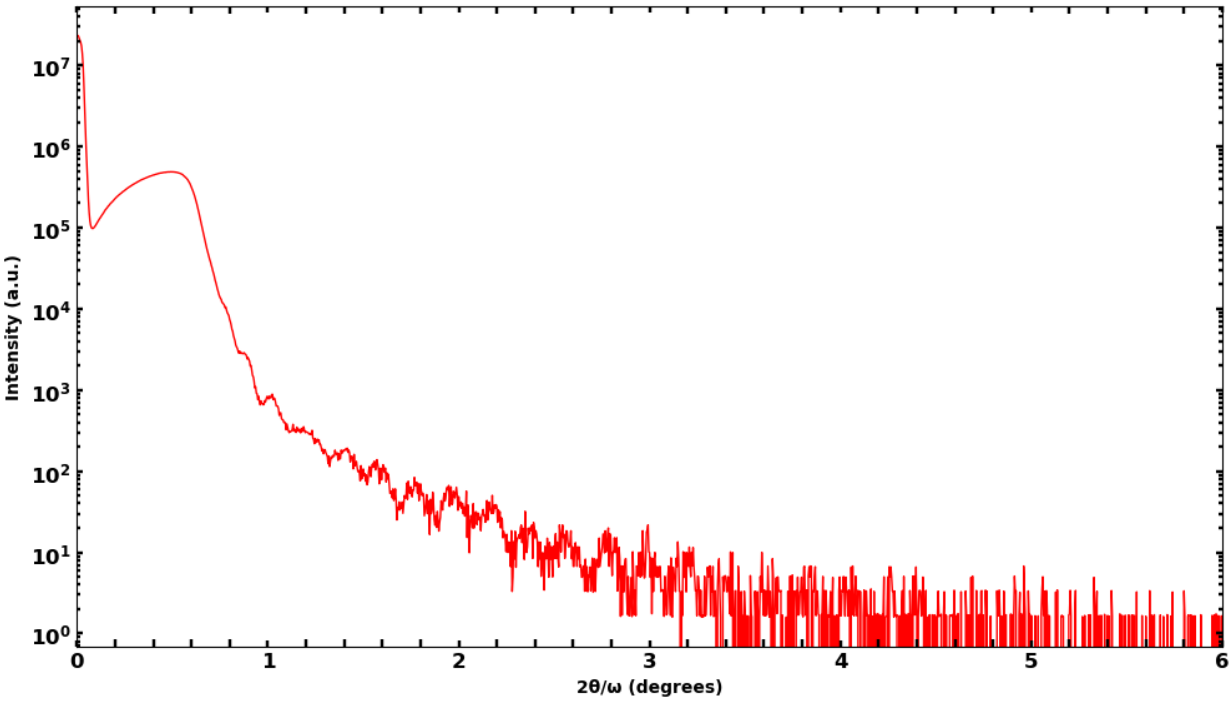

Figure 70:XRR scan of LSCF LSGM Heterostructure grown at 800°C and 150mTorr